


Article

Optimizing the Location of the Piezoelectric Actuator and Analyzing Its Effect on the Dynamics of Asymmetric Flexible Spacecraft

Kai Cao, Renyuan Xie, Jianmin Zhou, Xiaowei Zhang, Jingji Wang and Shuang Li * 

College of Astronautics, Nanjing University of Aeronautics and Astronautics, Nanjing 211106, China; kaicao@nuaa.edu.cn (K.C.); powerboy977@163.com (R.X.); liutong8224@163.com (J.Z.); xtayihwfnh@163.com (X.Z.); yushanke007@163.com (J.W.)

* Correspondence: lishuang@nuaa.edu.cn; Tel.: +86-25-84896039

Abstract: To address the challenge of optimizing the placement of actuators on an asymmetric spacecraft continuum system, this paper develops a rigid–flexible electromechanical coupling dynamic model that integrates the interactions among rigidity, flexibility, and electromechanical coupling effects. The model is constructed using ordinary differential equations and partial differential equations (ODE–PDEs) and considers the effects of the installation position and physical characteristics (mass and stiffness) of the piezoelectric (PZT) actuator on an asymmetric flexible spacecraft continuum system. The proposed model aims to accurately capture the complex interactions among the rigid body, flexible appendages, and PZT actuators. Based on the developed model, the installation location of the actuators is optimized using a genetic algorithm with a hybrid optimization criterion. In the numerical simulations, the proposed optimization algorithm is employed to determine the optimal installation position for the actuators. Then, the influence of the actuator’s physical characteristics and installation position on the dynamic properties of the spacecraft and the performance of the control system is investigated. The numerical simulation results demonstrate that the optimization algorithm can effectively identify the appropriate actuator installation location for the desired application. Utilizing the actuator with the optimized position allows for effective vibration suppression while consuming less energy.

Keywords: piezoelectric actuators; asymmetric flexible spacecraft; optimal positioning; rigid–flexible electromechanical coupling; ordinary differential equations and partial differential equations (ODE–PDEs)



Citation: Cao, K.; Xie, R.; Zhou, J.; Zhang, X.; Wang, J.; Li, S. Optimizing the Location of the Piezoelectric Actuator and Analyzing Its Effect on the Dynamics of Asymmetric Flexible Spacecraft. *Aerospace* **2023**, *10*, 716. <https://doi.org/10.3390/aerospace10080716>

Academic Editor: Angelo Cervone

Received: 18 July 2023

Revised: 13 August 2023

Accepted: 14 August 2023

Published: 16 August 2023



Copyright: © 2023 by the authors. Licensee MDPI, Basel, Switzerland. This article is an open access article distributed under the terms and conditions of the Creative Commons Attribution (CC BY) license (<https://creativecommons.org/licenses/by/4.0/>).

1. Introduction

Due to the increasing complexity of space exploration missions, traditional spacecraft designs are insufficient in meeting the evolving requirements for extended exploration ranges, more severe operating environments, and prolonged operational lifetimes [1]. As a result, future spacecraft will adopt modular architectures characterized by substantial size, the capability to accommodate multiple payloads, and extended operational lifespans. In order to address the challenges of reducing launch costs and breaking the limitation of rocket capacity, the utilization of flexible materials is becoming increasingly prominent, with such materials contributing a growing proportion of the overall structure [2]. The incorporation of rigid–flexible coupling, and in some cases full flexibility, are the primary features of these novel spacecraft designs [3–5]. For instance, some spacecraft systems have flexible components, such as the solar arrays of space solar power stations (SSPSs), the tethering systems of tethered satellites, and the deployable thin-film antennas of large-scale space antennas. These components introduce flexible characteristics to the spacecraft, resulting in a rigid–flexible coupling dynamic behavior. Unlike spacecraft with predominantly rigid dynamic behavior, the vibrations of the flexible appendages of flexible spacecraft

cannot be ignored. If left unchecked, these vibrations have the potential to not only impact the accuracy of the operational missions in orbit but also lead to structural damage [6].

In recent years, there has been a significant focus on vibration suppression techniques for flexible spacecraft, both in practical engineering applications and academic research. Particularly, with the development of smart structures, active vibration control strategies have made remarkable progress [7,8]. In contrast to passive vibration control, active vibration control has the advantages of fast response speed, strong environmental adaptability, and more direct and effective control methods. As a result, active vibration control is more suitable for vibration suppression of flexible spacecraft working in complex and unpredictable space environments. Piezoelectric (PZT) smart materials, as commonly employed functional materials for sensors and actuators, are widely applied in the construction of various smart structures, such as large flexible space structures [9], aircraft chatter control [10], etc. It is foreseeable that PZT smart materials will retain an important role in vibration control of large flexible space spacecraft in the future.

In Ref. [11], the dynamics model of the whole thin-layer antenna structure was obtained through finite element method (FEM), and the optimal placements of the PZT actuators was found using the particle swarm algorithm with the controllability matrix as an optimization metric. Subsequently, the active vibration strategy is designed based on the linear quadratic regulator (LQR) method. However, it is noted that since the structure was modeled and assembled using the FEM, the influence of the internal properties of the PZT element on the overall structure was ignored. In Ref. [12], PZT fiber composites were employed as actuators for active vibration control of smart composite panels. The controllability matrix was adopted as the optimizing criterion, and the particle swarm algorithm was applied to optimize the parameters of the actuator, including size, position, and orientation on the panel. In Ref. [13], an optimal sensor placement method for health monitoring of deployable antenna modules in SSPS is proposed. To determine the optimal sensor placement configuration, a genetic algorithm (GA) is employed, which utilizes a combined fitness function based on the effective independence method and the effective interval index. In Ref. [14], an intelligent active structure with distributed actuators and sensors is introduced for a very large mesh reflector, and the FEM is used for the assembly of the mesh reflector frame. To evaluate the best positioning and velocity feedback gains of the actuators, two cascade optimization procedures are performed.

Although the aforementioned research has made significant contributions to the modeling of flexible spacecraft dynamics and the optimization of actuator layouts, it is important to address the limitations of their approaches. Discrete methods have been widely used to model flexible spacecraft dynamics in the above research, including FEM and assumed modal methods. While these methods allow for obtaining the system dynamic model easily and enable simple controller design that can effectively control the dominant low-frequency modes, they are prone to spillover effects during the modal truncation process. Ignoring the spillover effect in the design of vibration suppression controller, the control input may cause oscillations in the residual modes, resulting in actual system dispersion and affecting the stability of the spacecraft. Reducing spillover effects has therefore been the focus of research efforts [15]. By utilizing the coupling dynamics model that combines ordinary and partial differential equations (ODE–PDEs), the system is not discretized or simplified in the modeling process, and all the modes of the system can be accurately described. Therefore, the controller designed based on this model can essentially avoid the spillover effect.

In Ref. [16], an antisymmetric vibration model of a flexible satellite with symmetrical flexible appendages on both sides is established by coupled ODE–PDEs based on Hamilton's principle, and the boundary control is proposed to track the desired pitch angle and suppress the vibration of the flexible appendages simultaneously. In Ref. [17], PDEs are derived considering flexible satellites with multisectioned solar panels and elastic connections between the main hub and solar panels. In Ref. [18], for distributed control of

a group of flexible spacecraft to track the attitude of a virtual leader, the PDEs are used to describe the dynamics of each spacecraft with an appendage on one side.

The ODE–PDEs coupling dynamic model provides an accurate description of the modal state of the system, and the research on continuous system controller design based on the model has gained significant attention. However, there is a limited amount of research on the influence of actuator installation position and self-physical properties, such as mass, density, and bending stiffness, on vibration control in a continuous system. Based on the aforementioned research, many studies have investigated the optimization of actuator layout in discrete systems, including trusses [19,20], plates [21], beams [22], and membrane structures [11,23]. At the same time, few articles have been dedicated to the optimization of actuator layouts for a cantilever beam with end loads. In contrast, it is worth noting that actuator layout optimization in discrete systems often emphasizes selecting nodes of the finite element method (FEM) as actuator locations, while overlooking the consideration of actuator physical properties [11,15]. In some articles, the consideration of actuator size is presented, but the model still relies on the discrete method without performing an optimization search over the entire structural interval. Additionally, the effect of the asymmetry of the system on the dynamic properties has only been addressed in a few articles focused on continuous systems [24]. Meanwhile, the impact of unilateral actuator installation and asymmetric installation on two-sided flexible appendages has received little attention, resulting in a lack of understanding regarding their influence on system dynamics.

Therefore, to address the aforementioned problems, the main work of this paper is as follows:

1. Considering the self-physical properties and unilaterally installed on the flexible appendages of the actuator, the ODE–PDEs coupling dynamics model is derived for the rigid–flexible electromechanical coupled asymmetric flexible spacecraft.
2. We use GA to optimize the installation position of the PZT actuators on the cantilever beam with end loads. The optimization covers the entire continuous interval of the beam length.
3. We analyze how the installation position of the actuator and its own physical characteristics affect the asymmetric characteristics of the system. We also study how optimizing the actuator position can improve the control performance of the distributed controller.

This paper is divided into the following sections: Section 1 provides the introduction. Section 2 presents the system dynamics modeling, including the PZT actuator model and the rigid–flexible electromechanical dynamics model of the asymmetric spacecraft. The optimization criterion and the algorithm designed to optimize the PZT actuator layout are introduced in Section 3. Section 4 presents the numerical simulation to illustrate the effect of the actuator installation position on the characteristics of the asymmetric spacecraft dynamics and vibration control. Section 5 is the conclusion.

2. Dynamics of Asymmetric Flexible Spacecraft with Integrated PZT Actuator

In this section, the dynamic model of the asymmetric flexible spacecraft is derived considering the electromechanical characteristics of the actuator. This research focuses on an asymmetric flexible spacecraft with slender flexible appendages, as depicted in Figure 1. To streamline the modeling process, the flexible spacecraft is simplified to include a central hub, flexible appendages with embedded PZT actuators on both sides, and the corresponding end loads of the flexible appendages. $O_1 - x_1y_1$ is the inertial frame, and the center of the central hub coincides with the origin O_1 at the initial moment. $O_2 - x_2y_2$ is the body reference frame fixed on the central hub, and the origin O_2 coincides with the center of the central hub. $O_3 - x_3y_3$ and $O_4 - x_4y_4$ are the local reference frame with the origin O_3 , O_4 at the point where the flexible appendages attach to the central hub. The central hub has a mass of M and a moment of inertia J . The lengths of the right and left flexible appendages are L_1 , L_2 , respectively. The attitude angular of the central hub, denoted as

θ , represents the change in the angle between the body reference frame $O_2 - x_2y_2$ and the inertial frame $O_1 - x_1y_1$. The width, height, linear density, and Young's modulus of the left and right flexible appendages are the same for both and are w_b, h_b, ρ_b, E_b , respectively. The end load masses of the right and left flexible appendage are M_1, M_2 , respectively. ξ_1, ξ_2 are the elastic deformation of the right and the left flexible appendages with respect to the local reference frame $O_3 - x_3y_3$ and $O_4 - x_4y_4$ at the position x and time t , respectively. A noteworthy point is that the $O_4 - y_4$ axis in the local coordinate system $O_4 - x_4y_4$ aligns with the $O_3 - y_3$ axis in the local coordinate system $O_3 - x_3y_3$. This is carried out to more accurately capture the vibration of the flexible appendages.

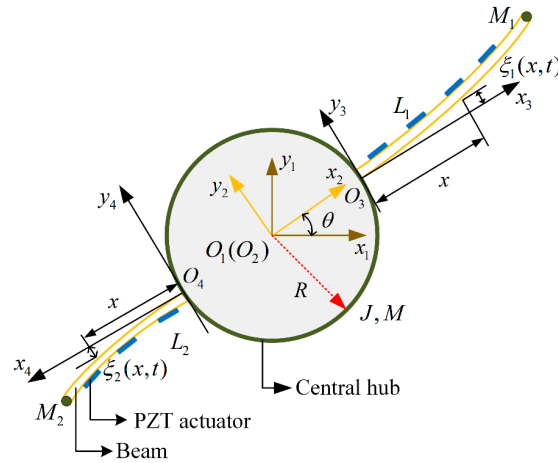


Figure 1. Diagram of asymmetric flexible spacecraft with embedded PZT actuator.

2.1. Actuator Model

Figure 2 shows the sectional view of the flexible appendage with embedded PZT actuator. In the figure, the $o - xz$ plane represents the section along the beam axis, and the $o - yz$ plane represents the section perpendicular to the axis. As shown in Figure 1, the flexible appendage is assumed to be a flexible beam with length L_i ($i = 1, 2$), height h_b , and width w_b . And the PZT actuator pieces are assumed to fit perfectly into the flexible appendage, and the width is the same as the flexible beam. The length, width, height, linear density, and Young's modulus of the PZT actuator pieces are $l_p, w_b, h_p, \rho_p, E_p$, respectively. The flexible beam with PZT actuators attached is regarded as a locally composite beam (LCB). Recalculating the physical properties of the LCB becomes imperative due to the modification induced by incorporating PZT actuators. The presence of these actuators alters significant characteristics, including density and bending stiffness, necessitating a reassessment of the LCB's physical properties.

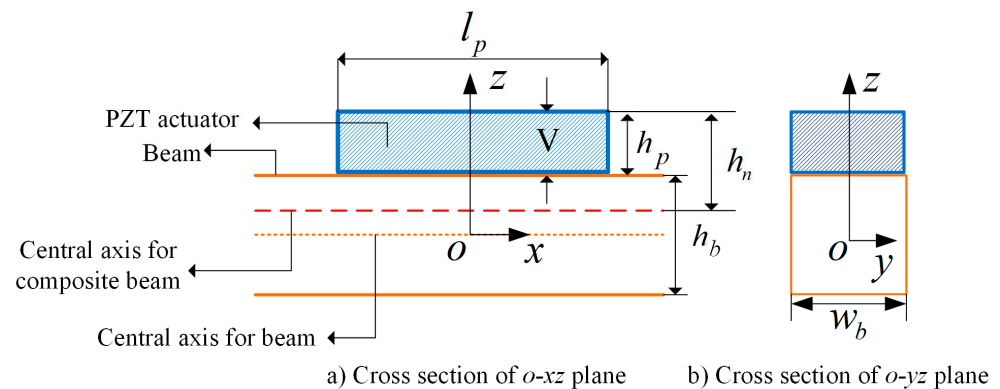


Figure 2. Cross-section of flexible appendage with embedded PZT actuator.

The linear density of the LCB is related to the installation position of the PZT actuator. The equation governing the linear density of the LCB is as follows:

$$\rho_c(x) = \rho_b + f(x)\rho_p \tag{1}$$

where

$$f(x) = \begin{cases} 1, & \text{if PZT is attached at } x \\ 0, & \text{others} \end{cases} \tag{2}$$

The neutral axis position of the LCB is determined through the utilization of the weighted average method. The equation for calculating the neutral axis position using the weighted average method is presented as follows:

$$z_c = \frac{\sum_{i=1}^n E_i S_{Zi}}{\sum_{i=1}^n E_i A_i} \tag{3}$$

where E_i represents the Young’s modulus of the structure i , S_{Zi} is the first moment of area of the structure i , A_i is the cross-sectional area of the structure i , and z_c is the neutral axis position. According to Equation (3), the neutral axis position of LCB can be calculated as follows:

$$\begin{aligned} h_n &= \frac{\frac{1}{2}w_b E_p h_p h_p + w_b E_b h_b (h_p + \frac{1}{2}h_b)}{E_p (h_p w_b) + E_b (h_b w_b)} \\ &= \frac{E_p h_p^2 + E_b h_b (h_b + 2h_p)}{2(E_p h_p + E_b h_b)} \end{aligned} \tag{4}$$

After determining the neutral axis position of the LCB, the moment of inertia of an area of the composite beam can be calculated using the parallel axis theorem. This calculation allows for the determination of the bending stiffness of the LCB.

The moment of inertia of an area of the composite beam is calculated as

$$\begin{aligned} I_b &= \frac{w_b h_b^3}{12} \\ I_{bn} &= \frac{w_b h_b^3}{12} + w_b h_b (h_p + \frac{h_b}{2} - h_n)^2 \\ I_{pn} &= \frac{w_b h_p^3}{12} + w_b h_p (h_n - \frac{h_p}{2})^2 \end{aligned} \tag{5}$$

where I_b is the moment of inertia of an area of the LCB segment without the PZT actuator attached, and I_{bn} , I_{pn} are the moment of inertia of an area of the flexible beam and the PZT actuators piece on the LCB segment with the PZT actuator attached, respectively.

The bending stiffness of the LCB can be expressed as follows:

$$EI_c(x) = \begin{cases} E_b I_{bn} + E_p I_{pn}, & f(x) = 1 \\ E_b I_b, & f(x) = 0 \end{cases} \tag{6}$$

where $EI_c(x)$ is the bending stiffness of the LCB, and $f(x)$ is defined as Equation (2).

The electromechanical model of the PZT actuator is commonly utilized and is not described in detail in this paper. The equations of the electromechanical model of the PZT actuator are given below [25]:

$$\begin{aligned} M_{bi} &= c_i V_i \\ c_i &= \frac{6E_b^2 I_b E_p d_{zx} t_b (t_b + t_p)}{E_b^2 t_b^4 + 4E_b E_p t_b^3 t_p + 6E_b E_p t_b^2 t_p^2 + 4E_b E_p t_b t_p^3 + E_p^2 t_p^4} \end{aligned} \tag{7}$$

$$M_b = \sum_{i=1}^n c_i V_i (H(x - l_{1i}) - H(x - l_{2i})) \tag{8}$$

where c_i is the PZT coupling coefficient of the i -th PZT actuator. The parameter depends on the geometric parameters, the structural properties of the actuator, and Young’s modulus

of the composite beam. V_i is the voltage applied to the i -th PZT actuator. M_{bi} represents the torque generated by the i -th PZT actuator, and M_b represents the sum of the torques generated by all the PZT actuators on the LCB. The PZT coefficient d_{zx} is the ratio of strain in the x direction when an electric field is applied across the PZT in the z direction. The step function $H(x)$ is used in the electromechanical model of the PZT actuator and has an amplitude of one unit. It is defined as follows:

$$H(x) = \begin{cases} 1, & x \geq 0 \\ 0, & x < 0 \end{cases} \tag{9}$$

2.2. Dynamics of Asymmetric Flexible Spacecraft

This section focuses on deriving the dynamical model of the asymmetric flexible spacecraft using Hamilton’s principle. In this paper, it is assumed that the mass of the central rigid body is significantly larger than the mass of the flexible appendages. The flexible appendages on both sides are treated as Euler–Bernoulli beams, considering only the transverse vibrations.

For clarity, notations $f_x = \partial f / \partial x$, $f_{xx} = \partial^2 f / \partial x^2$, $f_{xxx} = \partial^3 f / \partial x^3$, $f_{xxxx} = \partial^4 f / \partial x^4$, $\dot{f} = \partial f / \partial t$, and $\ddot{f} = \partial^2 f / \partial t^2$ are used throughout this paper.

The kinetic energy of the system is denoted as E_k and includes the kinetic energy of the central hub, the kinetic energy of the LCB on both sides, and the kinetic energy of end loads attached to the LCB. Therefore, E_k can be expressed through the following equations:

$$\begin{aligned} E_k = & \frac{1}{2} J \dot{\theta}^2 + \frac{1}{2} M (\dot{X}^2 + \dot{Y}^2) \\ & + \frac{1}{2} \int_0^{L_1} \rho_1(x) \left[(x+R)^2 \dot{\theta}^2 + 2(x+R) \dot{\theta} \dot{\xi}_1(x,t) + \dot{\xi}_1^2(x,t) + \dot{X}^2 + \dot{Y}^2 \right] dx \\ & + \frac{1}{2} \int_0^{L_2} \rho_2(x) \left[(x+R)^2 \dot{\theta}^2 + 2(x+R) \dot{\theta} \dot{\xi}_2(x,t) + \dot{\xi}_2^2(x,t) + \dot{X}^2 + \dot{Y}^2 \right] dx \\ & + \frac{1}{2} M_1 \left[(L_1+R)^2 \dot{\theta}^2 + 2(L_1+R) \dot{\theta} \dot{\xi}_1(L_1,t) + \dot{\xi}_1^2(L_1,t) + \dot{X}^2 + \dot{Y}^2 \right] \\ & + \frac{1}{2} M_2 \left[(L_2+R)^2 \dot{\theta}^2 + 2(L_2+R) \dot{\theta} \dot{\xi}_2(L_2,t) + \dot{\xi}_2^2(L_2,t) + \dot{X}^2 + \dot{Y}^2 \right] \end{aligned} \tag{10}$$

where $\rho_1(x)$, $\rho_2(x)$ are the densities of the right and left composite beams, respectively. $\rho_1(x)$, $\rho_2(x)$ are related to the installation position of the actuator and can be calculated using Equation (1). X and Y represent the changes in position of the center of the central hub in the inertial system along the $O - X$ and $O - Y$ axes, respectively.

The potential energy of the system, denoted as E_p , is given by considering solely the elastic potential energy of the LCB while ignoring their gravitational potential energy. And E_p can be expressed using the following equations:

$$E_p = \frac{1}{2} \int_0^{L_1} EI_1(x) \xi_{1xx}^2 dx + \frac{1}{2} \int_0^{L_2} EI_2(x) \xi_{2xx}^2 dx \tag{11}$$

where $EI_1(x)$, $EI_2(x)$ are the bending stiffness of the right and left composite beams, respectively. Similarly, $EI_1(x)$, $EI_2(x)$ also depend on the installation position of the actuator and can be calculated using Equation (6).

The virtual work, denoted by W , is calculated by considering the three components of work performed by the external forces on the system: the control torque applied to the

central rigid body and the forces exerted by the right and left PZT actuators attached to the LCB on the beams. Thus, W can be expression as follows:

$$W = \int \tau d\theta + \int F_X dX + \int F_Y dY + \int_0^{L_1} \frac{M_{b1}^2(x, t)}{2E_b I_b} dx + \int_0^{L_2} \frac{M_{b2}^2(x, t)}{2E_b I_b} dx \quad (12)$$

Starting from Hamilton’s principle $\int (\delta E_k - \delta E_p + \delta W) dt = 0$ and substituting E_k, E_p, W , the governing equations and boundary conditions can be derived as follows:

$$\begin{aligned} 0 = & \tau - J\ddot{\theta} - \int_0^{L_1} \rho_1(x)(x + R)^2 \ddot{\theta} dx - \int_0^{L_1} \rho_1(x)(x + R) \ddot{\xi}_1(x, t) dx \\ & - \int_0^{L_1} \rho_1(x)(x + R) (\ddot{Y} \cos \theta - \dot{Y} \dot{\theta} \sin \theta - \ddot{X} \sin \theta - \dot{X} \dot{\theta} \cos \theta) dx \\ & - \int_0^{L_1} \rho_1(x) [(x + R) \dot{\theta} + \dot{\xi}_1(x, t)] (\dot{Y} \sin \theta + \dot{X} \cos \theta) dx \\ & - \int_0^{L_2} \rho_2(x)(x + R)^2 \ddot{\theta} dx + \int_0^{L_2} \rho_2(x + R) \ddot{\xi}_2(x, t) dx \\ & + \int_0^{L_2} \rho_2(x)(x + R) (\ddot{Y} \cos \theta - \dot{Y} \dot{\theta} \sin \theta - \ddot{X} \sin \theta - \dot{X} \dot{\theta} \cos \theta) dx \\ & - \int_0^{L_2} \rho_2(x) [-(x + R) \dot{\theta} + \dot{\xi}_2(x, t)] (\dot{Y} \sin \theta + \dot{X} \cos \theta) dx \\ & - M_1(L_1 + R) [(L_1 + R) \ddot{\theta} + \ddot{\xi}_1(L_1, t)] \\ & - M_1(L_1 + R) (\ddot{Y} \cos \theta - \dot{Y} \dot{\theta} \sin \theta - \ddot{X} \sin \theta - \dot{X} \dot{\theta} \cos \theta) \\ & - M_1 [(L_1 + R) \dot{\theta} + \dot{\xi}_1(L_1, t)] (\dot{Y} \sin \theta + \dot{X} \cos \theta) \\ & + M_2(L_2 + R) [-(L_2 + R) \ddot{\theta} + \ddot{\xi}_2(L_2, t)] \\ & + M_2(L_2 + R) (\ddot{Y} \cos \theta - \dot{Y} \dot{\theta} \sin \theta - \ddot{X} \sin \theta - \dot{X} \dot{\theta} \cos \theta) \\ & - M_2 [-(L_2 + R) \dot{\theta} + \dot{\xi}_2(L_2, t)] (\dot{Y} \sin \theta + \dot{X} \cos \theta) \end{aligned} \quad (13)$$

$$\begin{aligned} 0 = & F_X - M\ddot{X} - M_1\ddot{X} - M_2\ddot{X} - \int_0^{L_1} \rho_1(x) dx \ddot{X} - \int_0^{L_2} \rho_2(x) dx \ddot{X} \\ & + \int_0^{L_1} \rho_1(x) [(x + R) \dot{\theta} + \dot{\xi}_1(x, t)] \dot{\theta} \cos \theta + \rho_1(x) [(x + R) \ddot{\theta} + \ddot{\xi}_1(x, t)] \sin \theta dx \\ & + \int_0^{L_2} \rho_2(x) [-(x + R) \dot{\theta} + \dot{\xi}_2(x, t)] \dot{\theta} \cos \theta + \rho_2(x) [-(x + R) \ddot{\theta} + \ddot{\xi}_2(x, t)] \sin \theta dx \\ & + M_1 [(L_1 + R) \dot{\theta} + \dot{\xi}_1(L_1, t)] \dot{\theta} \cos \theta + M_1 [(L_1 + R) \ddot{\theta} + \ddot{\xi}_1(L_1, t)] \sin \theta \\ & + M_2 [-(L_2 + R) \dot{\theta} + \dot{\xi}_2(L_2, t)] \dot{\theta} \cos \theta + M_2 [-(L_2 + R) \ddot{\theta} + \ddot{\xi}_2(L_2, t)] \sin \theta \end{aligned} \quad (14)$$

$$\begin{aligned} 0 = & F_Y - M\ddot{Y} - M_1\ddot{Y} - M_2\ddot{Y} - \int_0^{L_1} \rho_1(x) dx \ddot{Y} - \int_0^{L_2} \rho_2(x) dx \ddot{Y} \\ & + \int_0^{L_1} \rho_1(x) [(x + R) \dot{\theta} + \dot{\xi}_1(x, t)] \sin \theta \dot{\theta} - \rho_1(x) [(x + R) \ddot{\theta} + \ddot{\xi}_1(x, t)] \cos \theta dx \\ & + \int_0^{L_2} \rho_2(x) [-(x + R) \dot{\theta} + \dot{\xi}_2(x, t)] \sin \theta \dot{\theta} - \rho_2(x) [-(x + R) \ddot{\theta} + \ddot{\xi}_2(x, t)] \cos \theta dx \\ & + M_1 [(L_1 + R) \dot{\theta} + \dot{\xi}_1(L_1, t)] \dot{\theta} \sin \theta - M_1 [(L_1 + R) \ddot{\theta} + \ddot{\xi}_1(L_1, t)] \cos \theta \\ & + M_2 [-(L_2 + R) \dot{\theta} + \dot{\xi}_2(L_2, t)] \dot{\theta} \sin \theta - M_2 [-(L_2 + R) \ddot{\theta} + \ddot{\xi}_2(L_2, t)] \cos \theta \end{aligned} \quad (15)$$

$$\begin{aligned}
0 &= \int_0^{L_1} -\rho_1(x)[(x+R)\ddot{\theta} + \ddot{\xi}_1(x,t)]dx \\
&+ \int_0^{L_1} -\rho_1(x)(\ddot{Y}\cos\theta - \dot{Y}\dot{\theta}\sin\theta - \ddot{X}\sin\theta - \dot{X}\dot{\theta}\cos\theta)dx \\
&- \int_0^{L_1} EI_1(x)\xi_{1xxxx}dx + \int_0^{L_1} M_{b1}(x,t)_{xx}dx
\end{aligned} \tag{16}$$

$$\begin{aligned}
0 &= \int_0^{L_2} -\rho_2(x)[-(x+R)\ddot{\theta} + \ddot{\xi}_2(x,t)]dx \\
&+ \int_0^{L_2} -\rho_2(x)(\ddot{Y}\cos\theta - \dot{Y}\dot{\theta}\sin\theta - \ddot{X}\sin\theta - \dot{X}\dot{\theta}\cos\theta)dx \\
&- \int_0^{L_2} EI_2(x)\xi_{2xxxx}dx + \int_0^{L_2} M_{b2}(x,t)_{xx}dx
\end{aligned} \tag{17}$$

$$\begin{aligned}
&\xi_1(0,t) = \xi_2(0,t) = 0 \\
&\xi_{1x}(0,t) = \xi_{2x}(0,t) = 0 \\
&\xi_{1xx}(L_1,t) = \xi_{2xx}(L_2,t) = 0 \\
&M_1(\ddot{Y}\cos\theta - \dot{Y}\dot{\theta}\sin\theta - \ddot{X}\sin\theta - \dot{X}\dot{\theta}\cos\theta) \\
&= EI_1(L_1)\xi_{1xxx}(L_1,t) - M_1[(L_1+R)\ddot{\theta} + \ddot{\xi}_1(L_1,t)] \\
&M_2(\ddot{Y}\cos\theta - \dot{Y}\dot{\theta}\sin\theta - \ddot{X}\sin\theta - \dot{X}\dot{\theta}\cos\theta) \\
&= EI_2(L_2)\xi_{2xxx}(L_2,t) - M_2[-(L_2+R)\ddot{\theta} + \ddot{\xi}_2(L_2,t)]
\end{aligned} \tag{18}$$

Equations (13)–(17) represent ODE–PDEs describing the dynamics of the system, while boundary conditions are given by Equation (18). It is important to emphasize that the controller design is not the main focus of this paper, and therefore, the specific details of the controller design can be obtained in Ref. [24]. Additionally, it should be noted that while the above formula indicates that the integration operation is carried out over the entire beam length, the presence of the piezoelectric actuator attachment introduces discontinuities in the relevant parameters along the integration interval. In practice, it involves segmental integration.

3. Optimal Placement of the PZT Actuators

The impact of the PZT actuator is primarily observed in the vibration equations (Equations (16) and (17)) of the flexible appendage, based on the system dynamics model. This impact in turn affects the motion of the central hub through the appendage–hub coupling. Therefore, it is reasonable to focus the actuator layout optimization specifically on the vibration equation of the flexible beams. For the sake of simplifying the optimization process, this section exclusively considers flexible beams with PZT actuators as the target for optimization and neglects the central body and the coupling effect. The overall impact on the asymmetrical flexible spacecraft is analyzed through numerical simulations in Section 4, after obtaining the results of the optimized actuator layout. It is worth noting that the actuator optimization layout algorithm proposed in this section can also be applied to other scenarios involving varying lengths of the flexible appendages and the number of actuators. In Section 4, the optimization algorithm presented in this section is employed to optimize the actuator layout for different cases.

3.1. Design of Optimization Criteria

The schematic distribution of PZT actuators on a flexible beam is illustrated in Figure 3. As shown in the figure, the PZT actuator is attached to the top surface of the flexible beam. The length of the flexible beam is L , and the mass of the end load is M . The length of the PZT actuator piece is l_p , and the distances between the left and right sides of the actuator and the fixed end of the flexible beam are $x_{i,1}$, $x_{i,1} + l_p$, respectively. When a voltage is

applied to the PZT actuator, the PDE for the Euler–Bernoulli beam transverse vibration governing equation is described as follows [26]:

$$\int_0^L \left[\frac{\partial^2}{\partial x^2} \left[EI(x) \frac{\partial^2 y(x,t)}{\partial x^2} \right] + \rho(x) \frac{\partial^2 y(x,t)}{\partial t^2} \right] dx = \int_0^L \frac{\partial^2 M_b(x)}{\partial x^2} dx \tag{19}$$

$$\begin{aligned} y(x,t) = 0, \frac{\partial y(x,t)}{\partial x} = 0, x = 0 \\ EI(x) \frac{\partial^2 y(x,t)}{\partial x^2} = 0, \frac{\partial}{\partial x} \left[EI(x) \frac{\partial^2 y(x,t)}{\partial x^2} \right] = M_t \frac{\partial^2 y(x,t)}{\partial t^2}, x = L \end{aligned} \tag{20}$$

where $EI(x)$ and $\rho(x)$ represent the bending stiffness and linearity density, respectively, of the composite beam, which are identical to those defined for EI_c and ρ_c ; $y(x,t)$ represents the vibration deformation of the Euler–Bernoulli beam with end load; M_b denotes the control torque exerted on the beam by the actuators; and M_t represents the mass of the end load. Equation (19) represents the transverse vibration equation for the beam, while Equation (20) describes the boundary condition for a cantilevered beam subjected to end load.

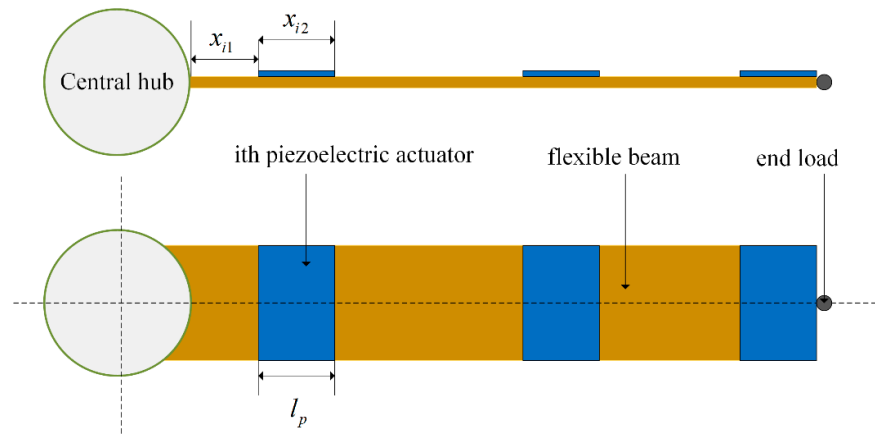


Figure 3. Schematic distribution of PZT actuators on a flexible beam.

Substituting Equation (8) into Equation (19), we can obtain the following equation:

$$\int_0^L \left[EI(x) \frac{\partial^4 y(x,t)}{\partial x^4} + \rho(x) \frac{\partial^2 y(x,t)}{\partial t^2} \right] dx = \int_0^L \sum_{i=1}^k c_i V_i \left[\ddot{H}(x - l_{i1}) - \ddot{H}(x - l_{i2}) \right] dx \tag{21}$$

According to the assumed mode method, the transverse vibration displacement of a flexible beam can be written as

$$y(x,t) = \sum_{i=1}^n \varphi_i(x) q_i(t) \tag{22}$$

where φ_i denotes the modal function of the i -th mode, while q_i denotes the modal coordinates of the i -th mode.

The orthogonality relations of modes for a cantilever beam with an end load are as follows:

$$\int_0^L \rho(x) \varphi_r(x) \varphi_s(x) dx + M_t \varphi_r(L) \varphi_s(L) = 0, r \neq s, \text{ and } r, s = 1, 2, \dots, n \tag{23}$$

Substituting Equations (22) and (23) into Equation (21), the decoupled system modes equations can be written as

$$\ddot{q}_i(t) + 2\gamma_i\omega_i\dot{q}_i(t) + \omega_i^2q_i(t) = \sum_{j=1}^k Q_{ij}, \quad (i = 1, 2, \dots, \infty, j = 1, 2, \dots, m) \quad (24)$$

where ω_i, γ_i represent the natural frequency and the coefficient of viscous damping of the i -th mode, respectively. Q_{ij} represents the component of the control force exerted by the j -th actuator on the beam in the i -th modal coordinates.

Therefore, the state space equation of the system is obtained from the mode decoupling Equation (24):

$$\dot{\mathbf{x}}(t) = \mathbf{A}\mathbf{x}(t) + \mathbf{B}\mathbf{V}(t) \quad (25)$$

where $\mathbf{x}(t) = [q_1(t), \dots, q_i(t), \dot{q}_1(t), \dots, \dot{q}_i(t)]^T$ and $\mathbf{V}(t) = [V_1(t), \dots, V_k(t)]^T$. It is noteworthy that the assumed modal model is employed for modal truncation in Equation (25). However, this model only serves the purpose of actuator position optimization and does not influence the continuous system controller or cause spillover effects.

Define the controllability matrix of the system as

$$W_c = \int_0^\infty e^{A\tau} B B^T e^{A^T\tau} d\tau \quad (26)$$

Therefore, the objective function for optimizing the actuator layout can be expressed as follows [27]:

$$\text{Crit} = \max[Q_1 \cdot \text{norm}(W_c) \cdot \text{trace}(W_c) \cdot \min(\text{svd}(W_c))] \rightarrow x_c \quad (27)$$

where $\text{norm}(W_c)$ corresponds to the criterion of minimum energy input, $\text{trace}(W_c)$ corresponds to the criterion of maximum energy transfer, and $\min[\text{svd}(W_c)]$ is related to the controllability of the system. And Q_1 is a constant used to keep the objective function within reasonable accuracy and adjust the weight of each factor.

3.2. Solution Approaches

GA has been widely utilized for optimizing actuator layouts in the field. Therefore, GA is also used in this section as an optimization algorithm to find optimal actuator positions. Since the dynamics equation of a flexible appendage with PZT actuators is a nonlinear equation, a nonlinear programming model has to be developed first for the configuration optimization of PZT actuators. We consider a flexible appendage of length L and a number of actuators n , which is to be determined according to the specific requirements of the task. The nonlinear programming model is

$$\begin{aligned} & \max f(\mathbf{x}) \\ \text{s.t.} & \begin{cases} x_1 \geq 0 \\ x_n + l_p \leq L, \quad 1 \leq i \leq n \\ x_i - x_{i-1} \geq l_p \end{cases} \end{aligned} \quad (28)$$

where $\mathbf{x} = [x_1, x_2, \dots, x_n] = [x_{11}, x_{21}, \dots, x_{n1}]$, $f(x) = \max[Q_1 \cdot \text{norm}(W_c) \cdot \text{trace}(W_c) \cdot \min(\text{svd}(W_c))]$, and $x_0 = 0$.

The flowchart of the optimization procedure conducted by the GA is presented in Figure 4. Given the parameters of the flexible appendage itself and the number of actuators to be optimized, the genetic algorithm is used to obtain the layout of these actuators on the flexible appendage.

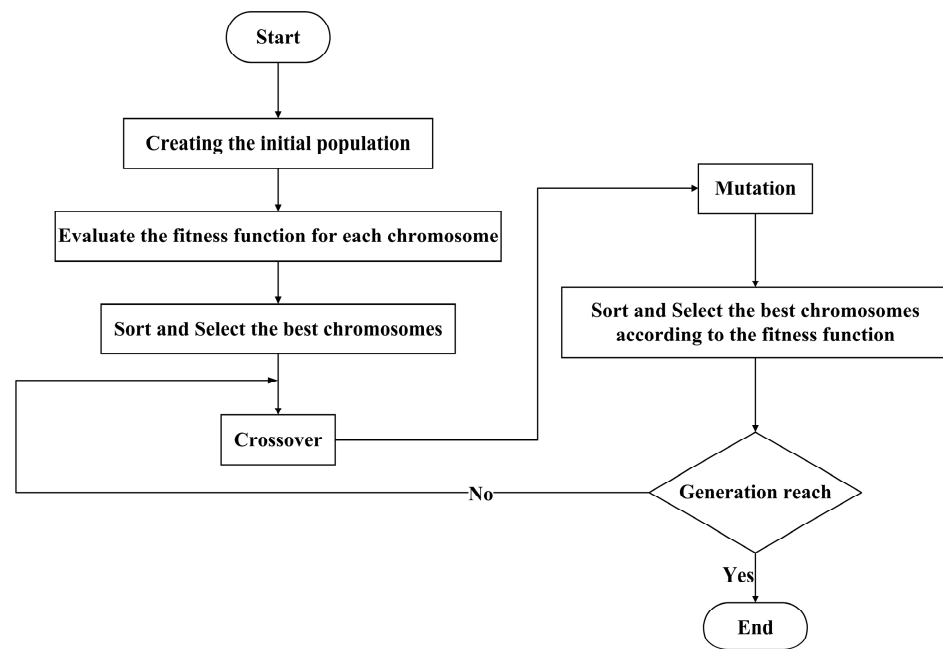


Figure 4. Flowchart of the GA.

4. Numerical Simulations

4.1. Actuator Position Optimization

This section showcases the results of employing GA for actuator placement optimization. For the sake of simulation simplification, this section focuses on only four simulation cases: (1) $L = 5$ m, $n = 1$; (2) $L = 5$ m, $n = 2$; (3) $L = 3$ m, $n = 1$; and (4) $L = 3$ m, $n = 2$, where L denotes the length of the beam, and n denotes the number of actuators. And the length of PZT actuators l_p is equal to 0.2 m in all cases. For optimization, a GA with the following configuration is considered in this paper: a population size of 200, a crossover fraction of 0.8, and a total of 150 generations. The remaining parameters of the flexible appendage are given in Table 1.

Table 1. The parameters of the flexible appendage.

Parameters	Value
Width (m)	0.05
Height (m)	0.035
Density ($\text{kg} \cdot \text{m}^3$)	6500
Damping	0.002

Figures 5 and 6 depict the iterative process of GA of Cases 1–4. As observed from the figure, the GA converges at around 20 generations of Case 1. The optimal installation position is approximately $x = 0$ m, and the corresponding optimal fitness value is approximately $J = -1.73$. From the figures, it can be observed that the iterative generation of Case 2 at convergence is around 60. The actuator installation positions converge to their optimal values, where the first actuator installation position is $x_1 = 0$ m and the second actuator installation position is $x_2 = 0.2$ m. The optimal fitness value for Case 2 is $J = -9.59$. The simulation results demonstrate that when the beam length is 5 m, the optimal actuator installation position is close to the root of the flexible beam, which aligns with the previous studies in Ref. [28].

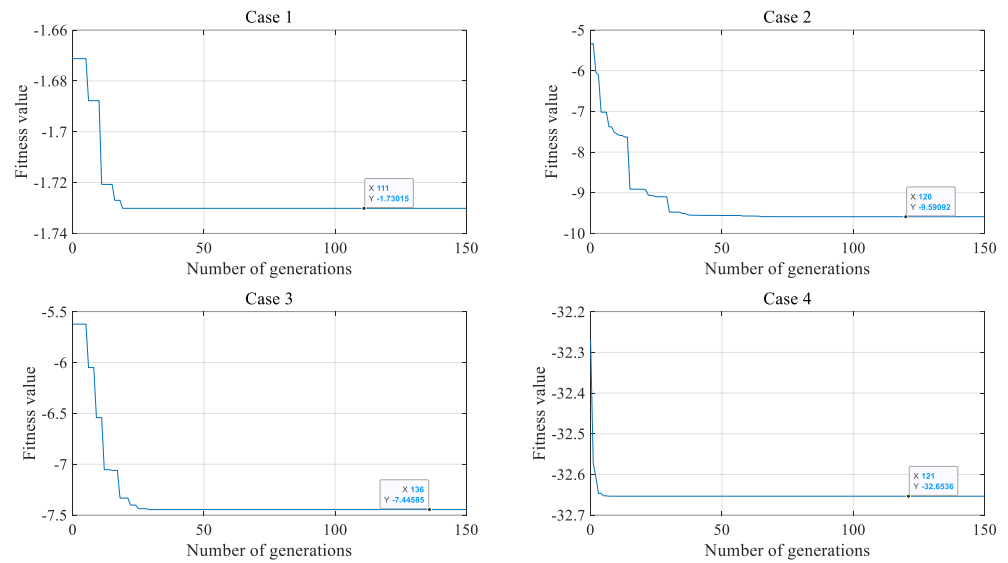


Figure 5. The iteration process of best fitness values in Case 1–4.

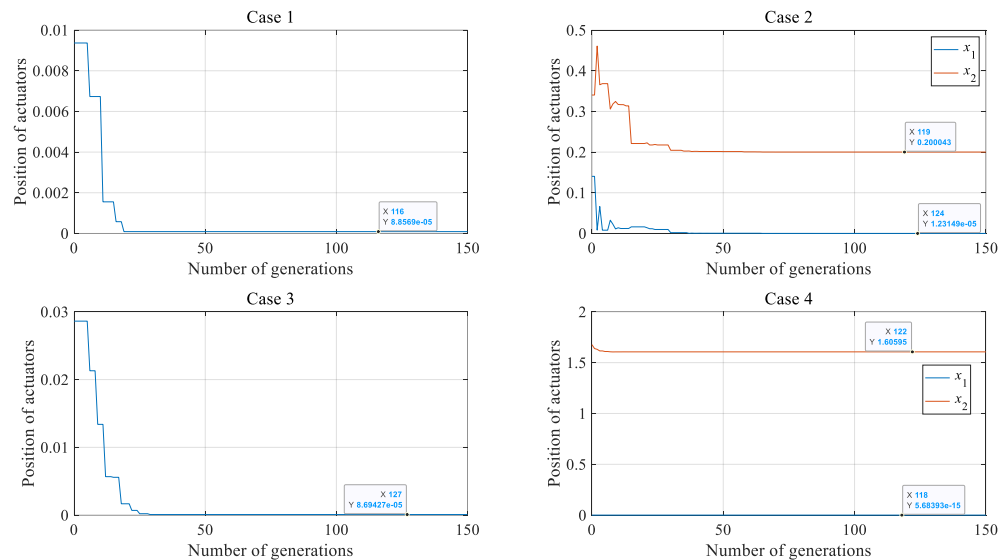


Figure 6. The iteration process of actuator positions in Cases 1–4.

When the length of the flexible appendage of Case 3 is changed to 3 m, it can be observed that the optimal installation position remains at the root of the flexible beam, yielding a best fitness value of $J = -7.445$. However, when the number of actuators is increased to two, the optimal installation position shifts away from the root of the flexible beam. And the best fitness value of Case 4 is $J = -32.65$, and the optimal installation positions for the two actuators are $x_1 = 0$ m and $x_2 = 1.606$ m. This discrepancy arises due to the chosen model of the flexible beam in this paper, which assumes a cantilever beam with a load at the end. As the beam length is altered, both the modal shape and modal frequencies undergo corresponding changes. Shortening the beam length intensifies the influence of the end load on the cantilever beam, thus altering its dynamic characteristics. Consequently, the optimization results deviate from those of Case 2, indicating the impact of beam length on the optimal outcomes. The optimization results for the best fitness value and the optimal actuator installation position in all of cases are summarized in Table 2.

Table 2. Genetic algorithm optimization results.

Case Number	Optimal Installation Position	Optimal Fitness Value
1	$J = -1.73$	$x = 0$ m
2	$J = -9.59$	$x_1 = 0$ m, $x_2 = 0.2$ m
3	$J = -7.445$	$x = 0$ m
4	$J = -32.65$	$x_1 = 0$ m, $x_2 = 1.606$ m

4.2. Influence of Actuator Position on Dynamic Characteristics

In this section, the influence of the installation position of the PZT actuator on the dynamic characteristics of the system is investigated, while considering the properties of the PZT actuator. The number of PZT actuators is considered as $n = 1$. In order to comprehensively demonstrate the influence of the actuator installation position and its properties on the dynamics characteristic of the system, this section involves the design of 8 flexible beams. The beams are categorized as follows:

1. Beam 1: This beam has no actuator attached, and its length is $L = 5$ m.
2. Beams 2–4: These beams also have a length of $L = 5$ m and the actuators are installed at positions $x = 4.8$ m, $x = 2.4$ m, and $x = 0$ m, respectively.
3. Beam 5: Similar to Beam 1, this beam has no actuator, but its length is changed to $L = 3$ m.
4. Beams 6–8: These beams have a length of $L = 3$ m and the actuators are installed at positions $x = 2.8$ m, $x = 1.4$ m, and $x = 0$ m, respectively.

By conducting experiments on these beams, we can thoroughly examine and analyze the effects of actuator installation position and properties on the dynamic characteristics of the system. Due to the difference in installation position of the actuator, the original modal shape function of the flexible beam is no longer applicable. Therefore, for different installation positions, firstly, the modal shape function and modal frequency need to be derived. The modal equations for all beams are provided in Appendix A.

Based on the above beam parameters, the following cases were designed for a symmetrical configuration:

1. The flexible appendages on both sides of the central hub are symmetrically configured with a length of $L_1 = L_2 = 5$ m, and there is no actuator attached.
2. The flexible appendages on both sides of the central hub are symmetrically configured with a length of $L_1 = L_2 = 5$ m, and the actuators are installed at the root $x = 0$ m.
3. The flexible appendages on both sides of the central hub are symmetrically configured with a length of $L_1 = L_2 = 5$ m, and the actuators are installed at the middle point $x = 2.4$ m.
4. The flexible appendages on both sides of the central hub are symmetrically configured with a length of $L_1 = L_2 = 5$ m, and the actuators are installed at the end point $x = 4.8$ m.

The cases for asymmetric configuration are as follows:

5. The flexible appendages on both sides of the central hub are asymmetrically configured with lengths of $L_1 = 5$ m and $L_2 = 3$ m, respectively, with no actuator attached.
6. The flexible appendages on both sides of the central hub are asymmetrically configured with lengths of $L_1 = 5$ m and $L_2 = 3$ m, respectively, with the actuators installed at the root $x = 0$ m.
7. The flexible appendages on both sides of the central hub are asymmetrically configured with lengths of $L_1 = 5$ m and $L_2 = 3$ m, respectively, and the actuators are installed at the middle points $x = 2.4$ m and $x = 1.4$ m, respectively.
8. The flexible appendages on both sides of the central hub are asymmetrically configured with lengths of $L_1 = 5$ m and $L_2 = 3$ m, respectively, with the actuators installed at the end points $x = 4.8$ m and $x = 2.8$ m, respectively.

Table 3 summarizes the parameter settings for Cases 1–8. Additionally, Table 4 provides the parameter values for the central hub, the flexible appendages, and the actuator. Furthermore, Table 5 displays the initial conditions for the system's free vibration. The simulation results of the system's free vibration are shown in the Figures 7–16.

Table 3. Parameter settings for all cases.

Case Number	Length of the Right Beam	Length of the Left Beam	Actuator Installation Position on the Right Beam	Actuator Installation Position on the Left Beam
1	5 m	5 m	No Actuator	No Actuator
2	5 m	5 m	0 m	0 m
3	5 m	5 m	2.4 m	2.4 m
4	5 m	5 m	4.8 m	4.8 m
5	5 m	3 m	No Actuator	No Actuator
6	5 m	3 m	0 m	0 m
7	5 m	3 m	2.4 m	1.4 m
8	5 m	3 m	4.8 m	2.8 m

Table 4. Parameters value of the system.

Component	Material Property	Value
Central hub	Mass (kg)	200
	Radius (m)	2
	Moment of inertia (kg·m ²)	160
Flexible beam	Young's modulus (GPa)	0.689
	Width (m)	0.05
	Height (m)	0.035
	Density (kg/m ³)	6500
PZT actuator	Young's modulus (GPa)	0.63
	Length (m)	0.2
	Width (m)	0.05
	Height (m)	0.005
	Density(kg/m ³)	7650
	d_{zx} (m/V)	1×10^{-12}

Table 5. Initial conditions of the system.

$\theta(0)$	$\dot{\theta}(0)$	$X(0)$	$\dot{X}(0)$	$Y(0)$	$\dot{Y}(0)$	$q_{11}(0)$	$q_{12}(0)$	$q_{21}(0)$	$q_{22}(0)$	$\dot{q}_{11}(0)$	$\dot{q}_{12}(0)$	$\dot{q}_{21}(0)$	$\dot{q}_{22}(0)$
0	0	0	0	0	0	0.2	0.02	0.2	0.02	0	0	0	0

In Cases 1–4, it is important to note that the initial amplitudes and phases for the vibration of the flexible beams on both sides are assumed to be equal. Additionally, the flexible appendages on both sides are symmetrically configured, satisfying the condition of symmetrical vibration. As depicted in Figures 7–11, it is evident that under the condition of symmetrical vibration, the amplitudes and phases of the flexible beams on both sides remain the same throughout the entire vibration process. Furthermore, the attitude of the central hub exhibits minimal variations. Simultaneously, the attitude of the central hub exhibits minimal variations of approximately 10^{-3} rad, with negligible oscillation along the OX axis, measuring around 10^{-4} m. However, vibrations along the OY axis are observed with a maximum amplitude of 0.06 m. This observation aligns with the phenomenon of symmetrical vibration previously documented in earlier studies [24].

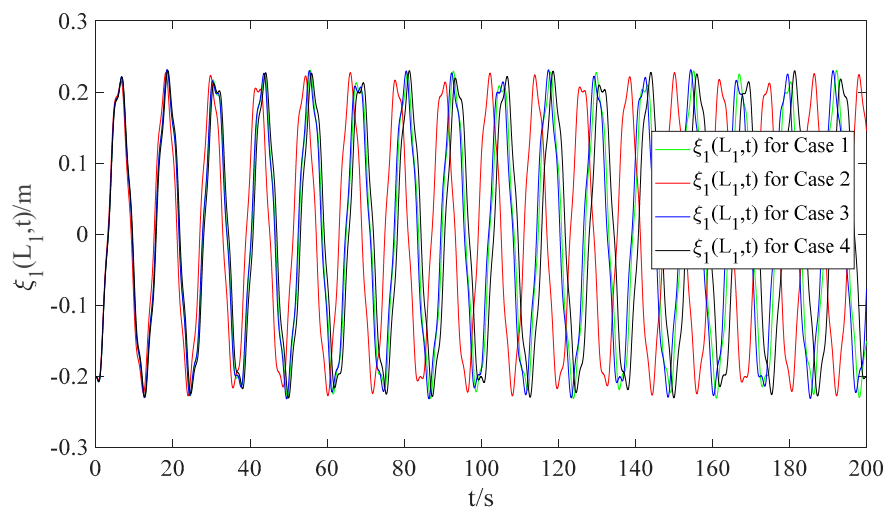


Figure 7. Vibration displacement of the end point of the right flexible beam for Cases 1–4.

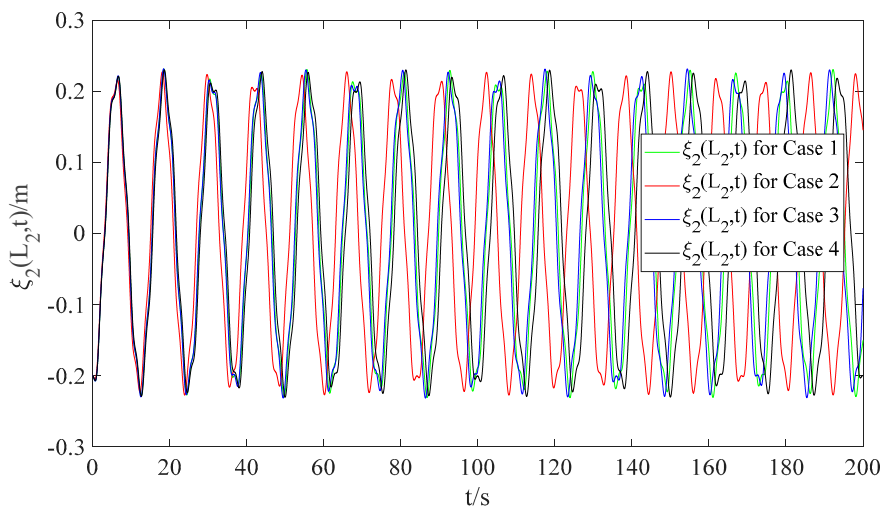


Figure 8. Vibration displacement of the end point of the left flexible beam for Cases 1–4.

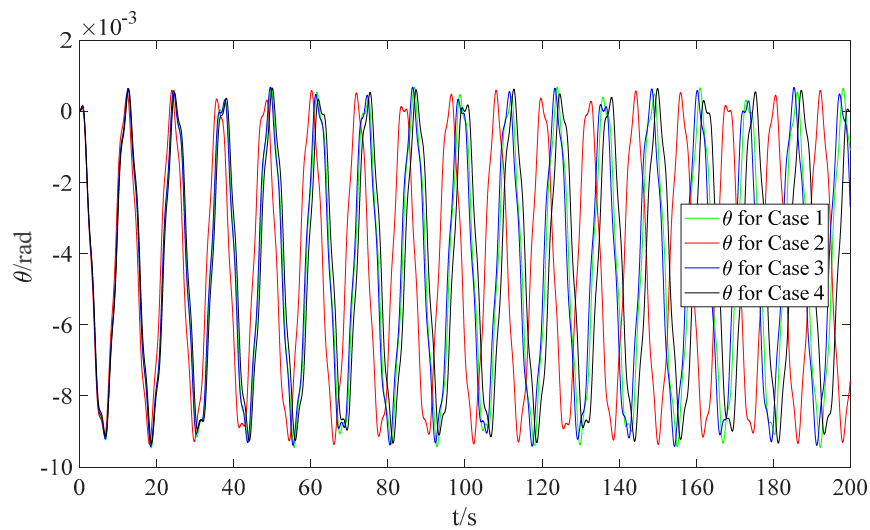


Figure 9. Angle of the central hub for Cases 1–4.

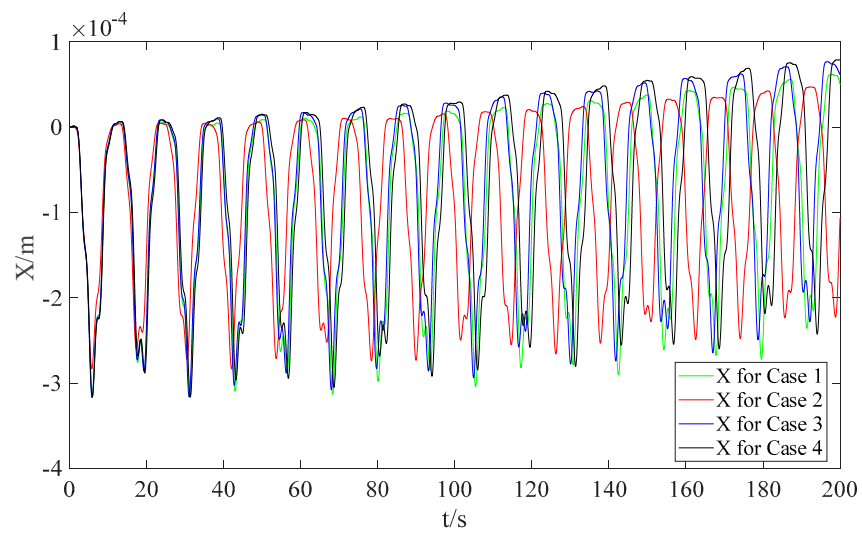


Figure 10. Displacement of the central hub in X-direction for Cases 1–4.

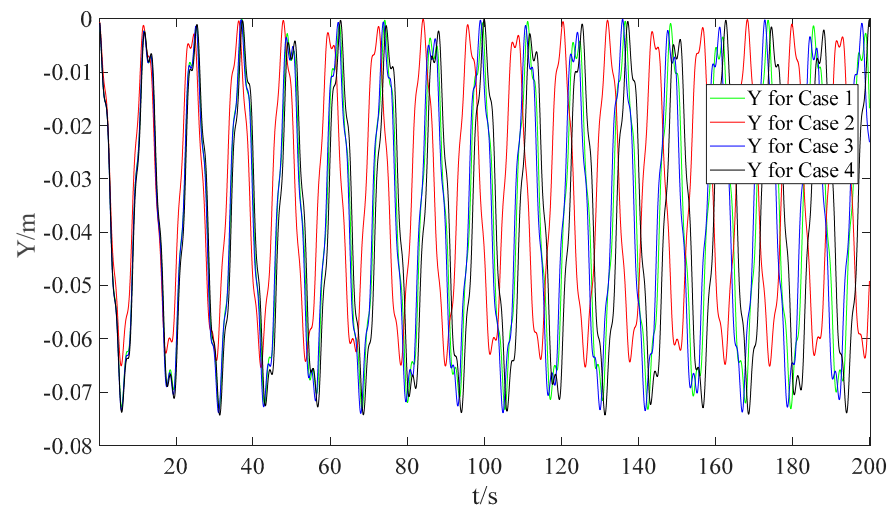


Figure 11. Displacement of the central hub in Y-direction for Cases 1–4.

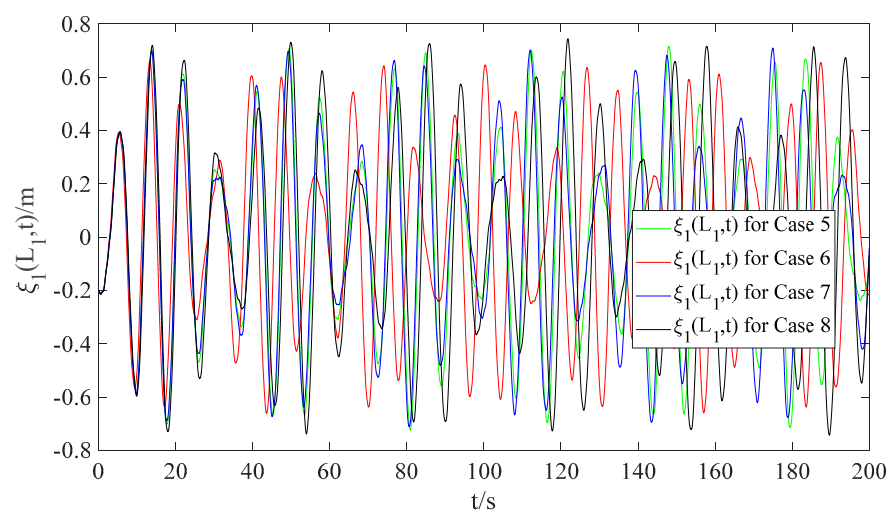


Figure 12. Vibration displacement of the end point of the right flexible beam for Cases 5–8.

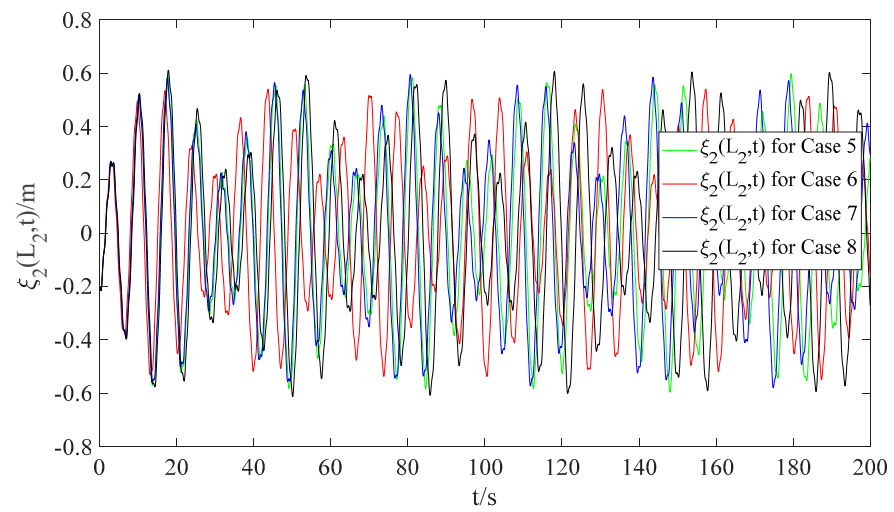


Figure 13. Vibration displacement of the end point of the left flexible beam for Cases 5–8.

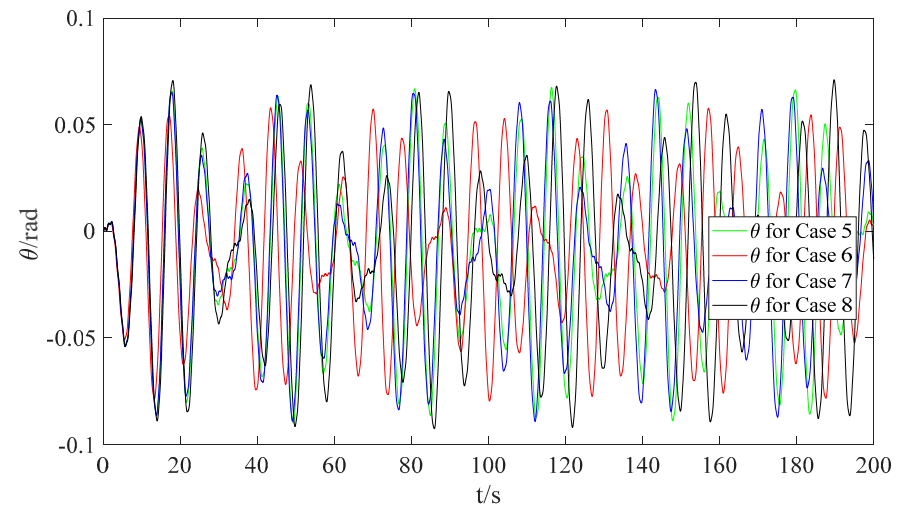


Figure 14. Angle of the central hub for Cases 5–8.

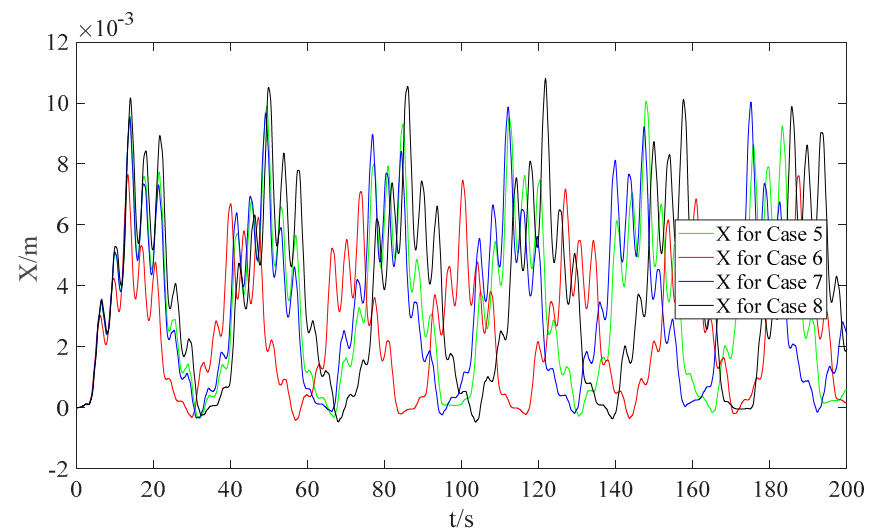


Figure 15. Displacement of the central hub in X-direction for Cases 5–8.

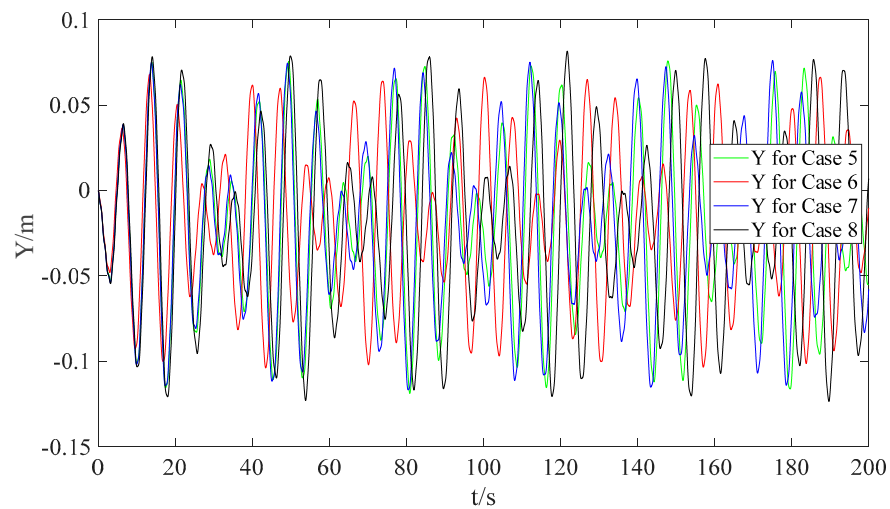


Figure 16. Displacement of the central hub in Y-direction for Cases 5–8.

Figures 7 and 8 display the vibration displacements of the end point of the flexible beams in Cases 1–4. The figures indicate that initially, the vibration amplitude and phase of all cases show similarities. However, as the simulation progresses, the vibration phase gradually shifts. Case 2 reaches its peak phase the earliest, followed by Case 1 and Case 3, while Case 4 exhibits the slowest phase progression. The phase difference between Case 1 and Case 3 is minimal. The observed variation in vibration phase is attributed to the changes in the natural frequency and modal equations of the LCB caused by the differences in the actuator installation position. While the actuator itself has a minimal impact on the natural frequency and modal equations of the LCB due to its small size, the accumulated phase shift gradually increases over time during the simulation. Additionally, Figures 9–11 present the changes in the attitude angle and positional oscillations of the central hub along the OX and OY axes. These figures demonstrate a similar phenomenon to the vibration displacements of the flexible beams. The vibration amplitudes remain largely consistent, while the vibration phases vary. Specifically, Case 2 exhibits the fastest phase, Case 4 displays the slowest phase, and Cases 1 and 3 have intermediate and closely aligned phases.

The faster phase observed in Case 2 can indeed be attributed to the installation of the actuator at the root of the flexible beam. This specific placement strengthens the root of the structure and enhances the bending stiffness at that particular location. As a result, the actuator absorbs relatively less energy from the vibration of the beam, leading to a faster phase. In Case 4, where the actuator is installed at the end of the flexible beam, the actuator absorbs a significant amount of vibration energy from the beam. Consequently, the vibrations in this case are in a slower phase compared with the other cases. In Case 1, where no actuator is installed, the phase falls in the middle of the two extreme cases (Case 2 and Case 4). In Case 3, the actuator is installed at the middle of the flexible beam. The energy absorption by the actuator in this case is relatively less, resulting in a phase that is not significantly different from that of Case 1. These differences in phase reflect the varying amounts of energy absorption by the actuators at different installation positions, thereby influencing the overall vibration characteristics of the system.

The impact of the actuator installation position on the system dynamics in an asymmetric configuration during free vibration is depicted in Figures 12–16. It is evident from Figures 12 and 13 that the vibration amplitudes and phases of the end point of the right and left beams no longer coincide when the flexible appendages on both sides are no longer symmetrical. As the right-side beam is longer than the left-side beam, its vibration amplitude is significantly larger, and its vibration phase is also faster compared with the left-side beam, assuming the initial amplitude is equal. The variation in the attitude angle of the central rigid body is depicted in Figure 14. It is evident from the figure that the attitude angle of the center hub no longer exhibits a sinusoidal function pattern but displays

a more pronounced uneven peak. Additionally, the positional oscillations of the central hub along the OX and OY axes are illustrated in Figures 15 and 16, respectively. From the figures, it can be observed that the maximum amplitude of the positional oscillation along the OX axis is 10^{-2} m, indicating a significant displacement of the central hub in that direction. Similarly, the positional oscillation along the OY axis reaches an amplitude of approximately 0.08 m. The observed phenomenon can be attributed to the asymmetric configuration of the system on both sides, which leads to an imbalance in the forces and torques exerted by the beams on the central rigid body.

Simultaneously, the phase of the left beam is slightly slower than that of the right beam, influenced by the physical characteristics of the actuator itself. The shorter length of the left beam results in a greater impact of the actuator on its structure. Additionally, it can be observed from the figure that the difference in actuator installation position in Cases 5–8 yields vibration phases similar to those in Cases 1–4. Specifically, Case 6 exhibits the fastest phase, Case 8 has the slowest phase, and Cases 5 and 7 fall in between with minimal difference. The reason behind this phenomenon is the same as in Cases 1–4. When the actuator is positioned at the root of the beam, it effectively reinforces the root, resulting in the fastest vibration phase. Conversely, when the actuator is installed at the end of the beam, it absorbs a larger amount of beam energy, leading to the slowest phase. For the remaining two cases, the difference in beam energy absorption is not significant, hence their vibration phases closely resemble each other.

4.3. Influence of Actuator Position on Control Performance

This section focuses on a single actuator as the research object and simulates and analyzes the influence of the optimized and unoptimized installation positions on the control performance. Based on the finding in Section 4.1, it is known that the optimal position is $x = 0$ m for $L = 5$ m. Therefore, this section selects Case 2 ($x = 0$ m) and Case 4 ($x = 4.8$ m) from Section 4.2 as the research object to analyze the effect on control performance. The same control parameters and initial conditions are adopted for both cases, and the controller is designed following the methodology outlined in Ref. [24], which is a distributed controller for a rigid–flexible coupled spacecraft continuum system that can avoid spillover effects. The control objective is to perform attitude maneuvers and vibration suppression simultaneously. The simulation's initial state settings are consistent with those presented in Section 4.2, as detailed in Table 5. The control objective is to achieve attitude maneuvering to an attitude angle of 0.02 rad while simultaneously performing vibration suppression of flexible appendages and position holding of the central rigid body. The simulation results are illustrated in Figures 17–24.

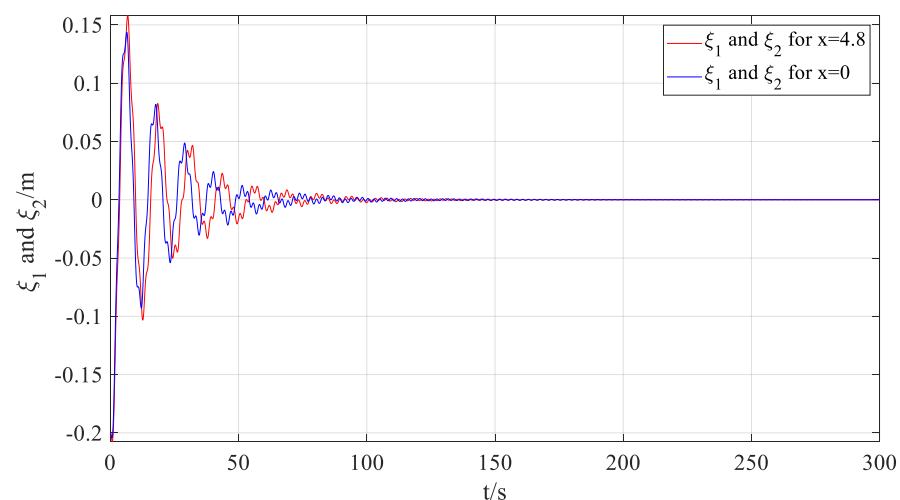


Figure 17. Vibration displacement of the end point of the right and left flexible beam.

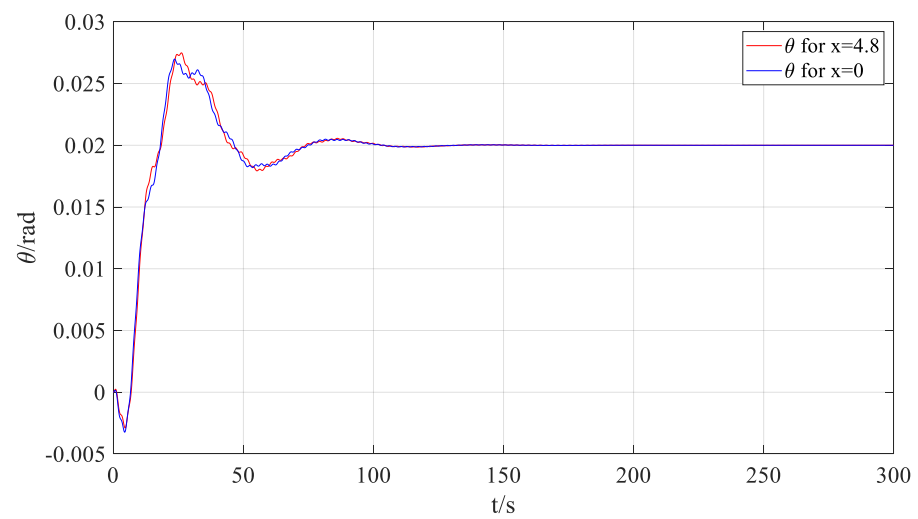


Figure 18. Angle of the central hub.

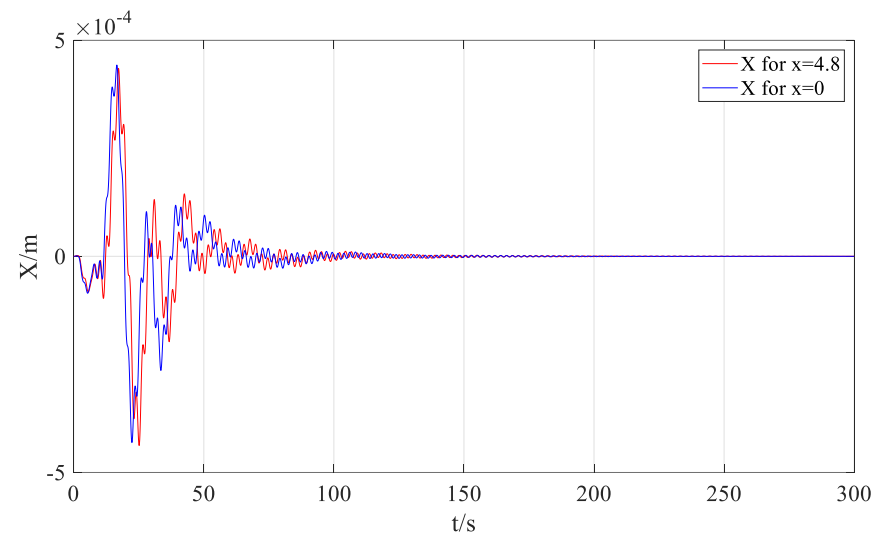


Figure 19. Displacement of the central hub in X-direction.

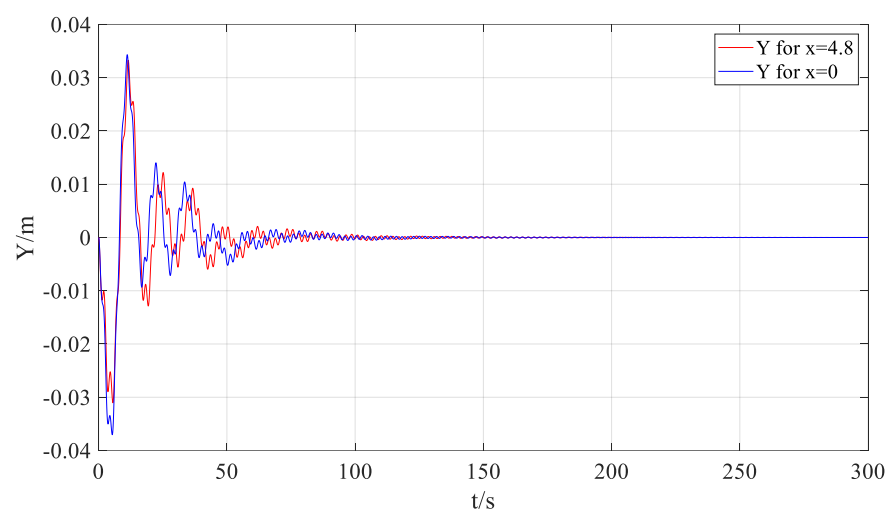


Figure 20. Displacement of the central hub in Y-direction.

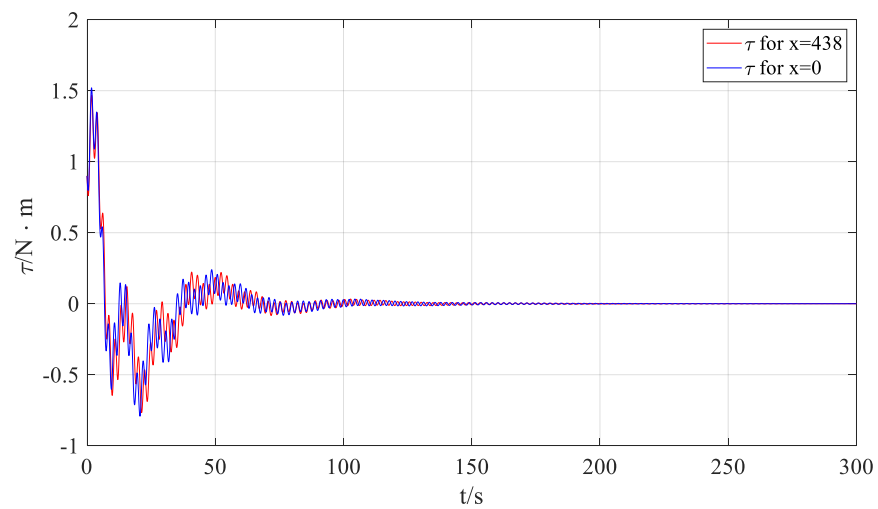


Figure 21. Control torque.

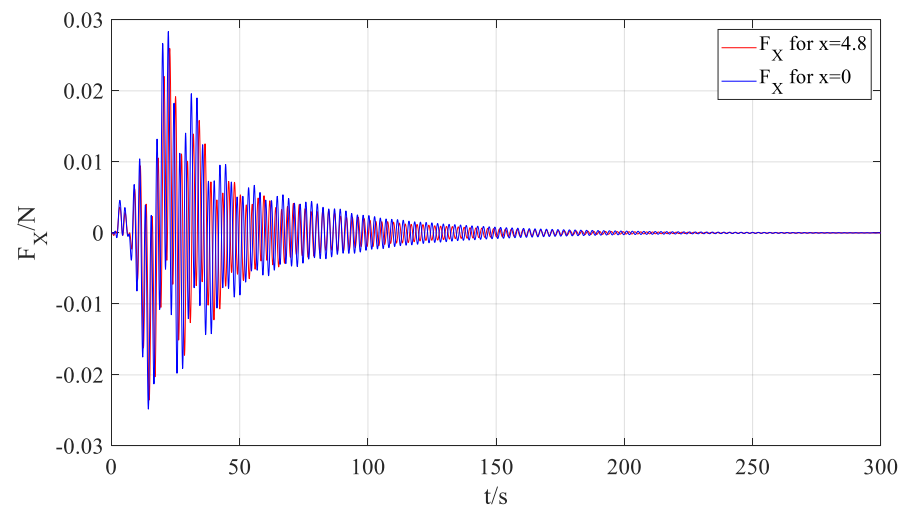


Figure 22. Control force applied on central hub along X-direction.

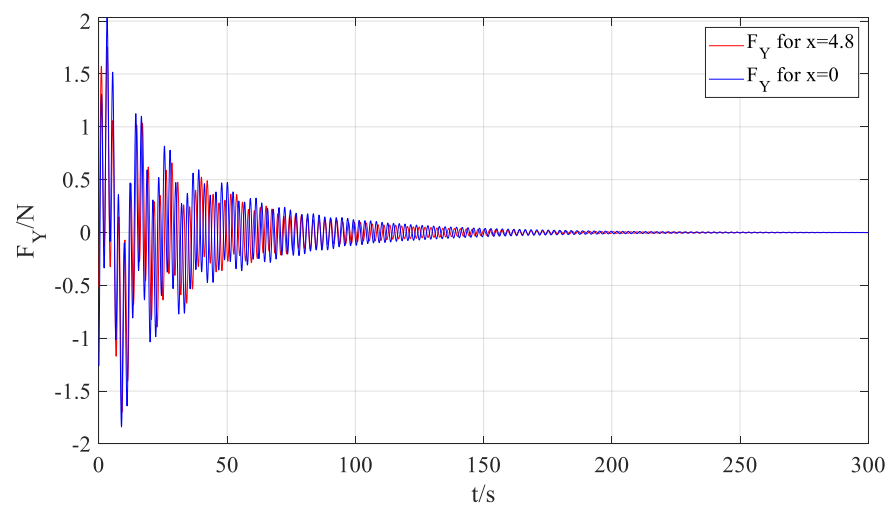


Figure 23. Control force applied on central hub along Y-direction.

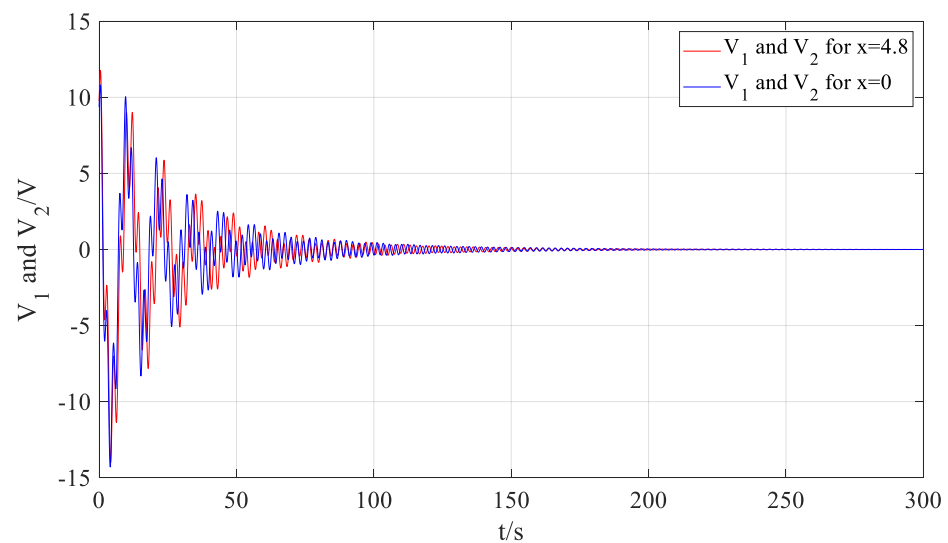


Figure 24. Output voltage of actuator embedded in flexible beam.

The control results for both cases are depicted in Figures 17–24. As demonstrated in Figures 17–20, simultaneous attitude maneuvering of the central hub and vibration suppression of the flexible beams can be achieved in both cases. Additionally, as the initial conditions satisfy the symmetric vibration condition, the vibration curves of the left and right flexible beams remain identical. However, the control performance with the optimized actuator installation position is slightly more effective than with the nonoptimized one, as evidenced by the lower vibration amplitude of the end point of the beams in the Figure 17. Figures 21–23 depict the curves of control force and torque applied to the central hub during attitude maneuvering and vibration suppression, while Figure 24 shows the curve of the input voltage of the PZT actuator over time. Due to the symmetrical configuration of the flexible beams on both sides and the use of the same controller and control parameters, the control voltage applied to the beams is the same on both sides. To provide a comprehensive demonstration of the energy consumption in both cases, the control force, control torque, and input voltage were integrated over a period of 300 s, and the results are presented in Table 6. The table clearly indicates that the control torque of the central hub and the input voltages of the actuators are lower when using the optimized actuator position. This observation highlights the effectiveness of control with the optimized actuator position, as it reduces the energy consumption required for vibration suppression of the flexible beam, aligning with the optimization objectives. At the same time, the control forces are higher compared with the nonoptimized position, particularly the control force in the Y-direction. This is attributed to the fact that placing the actuator at the root of the flexible beam effectively increases the mass of the central hub. As a result, in the symmetric vibration condition, the position of the central rigid body primarily oscillates along the Y-axis. Consequently, more energy is required to maintain the position of the central rigid body in the Y-axis direction. This further explains the higher control forces observed, especially in the Y-direction, when the actuator is placed at the root of the flexible beam.

Table 6. Energy consumption of control variables.

Integral Variables	Integral Value for Case 4	Integral Value for Case 2
τ (N · m)	19.0538	18.9485
F_X (N)	0.4857	0.5752
F_Y (N)	29.8984	34.7184
V_1 (V)	193.9818	190.8399
V_2 (V)	193.9818	190.8399

5. Conclusions

In this paper, a rigid–flexible electromechanical coupling dynamics model, accounting for the self-properties of the PZT actuator and its unilateral attachment to the flexible appendage, is developed for an asymmetric flexible spacecraft. The model is constructed using the distributed parameter method and the variational method, combining partial differential equations (PDEs) and ordinary differential equations (ODEs). Focusing on a loaded cantilever beam model, the actuator installation position is optimized using a genetic algorithm (GA) based on the controllability matrix design criterion. Notably, due to the specific characteristics of the loaded cantilever beam, the optimal actuator installation location obtained by the GA is not always at the root of the beam. Instead, it is determined in relation to the beam length and the end load mass. Through numerical simulations, the study investigates the impact of the actuator installation position on the asymmetric characteristics of the spacecraft and evaluates the influence of the optimized installation position on the control performance.

The simulation results demonstrate that the actuator installation position significantly affects the structural characteristics of the composite beam, subsequently influencing the vibration characteristics of the system. When the actuator installation position varies, the vibration phase is affected by this positioning, while the amplitude remains relatively constant. The optimization of the actuator position results in a slight reduction in energy consumption for vibration suppression. However, since the actuator is located at the root, leading to an increase in the mass of the rigid body, the control force exerted on the rigid body also increases, particularly in the Y -direction. In the case of large space structures, it is anticipated that the impact of optimizing the actuator position on the control performance will be more pronounced and beneficial.

Author Contributions: Conceptualization, K.C. and S.L.; methodology, K.C. and S.L.; software, K.C.; validation, K.C. and S.L.; formal analysis, K.C. and R.X.; investigation, K.C., J.Z., X.Z., J.W. and S.L.; resources, S.L.; data curation, K.C.; writing—original draft preparation, K.C. and S.L.; writing—review and editing, K.C., R.X., J.Z., X.Z., J.W. and S.L.; visualization, K.C.; supervision, S.L.; project administration, S.L.; funding acquisition, S.L. All authors have read and agreed to the published version of the manuscript.

Funding: This work was partially supported by the National Natural Science Foundation of China (Grant No. 11972182), and Postgraduate Research & Practice Innovation Program of Jiangsu Province (Grant No. KYCX21_0233). The authors fully appreciate their financial support.

Data Availability Statement: Not applicable.

Acknowledgments: The authors would like to thank the reviewers for their constructive comments and suggestions that may help improve this paper.

Conflicts of Interest: The authors declare that they have no known competing financial interests or personal relationships that could have appeared to influence the work reported in this paper.

Appendix A

1. Beam 1: No actuator, $L = 5$ m.

$$\begin{aligned}\varphi_{11} &= 0.60512 \cos(0.34763x) - 0.60512 \cosh(0.34763x) \\ &\quad - 0.44714 \sin(0.34763x) + 0.44714 \sinh(0.34763x) \\ \varphi_{12} &= 0.60512 \cos(0.88455x) - 0.60512 \cosh(0.88455x) \\ &\quad - 0.6153 \sin(0.88455x) + 0.6153 \sinh(0.88455x)\end{aligned}\tag{A1}$$

2. Beam 2: $x = 4.8$ m, $L = 5$ m.

$$\begin{aligned}
 \varphi_{11} &= 0.60894 \cos(0.34599x) - 0.60894 \cosh(0.34599x) \\
 &\quad - 0.45046 \sin(0.34599x) + 0.45046 \sinh(0.34599x) \\
 \varphi_{12} &= 0.60894 \cos(0.88253x) - 0.60894 \cosh(0.88253x) \\
 &\quad - 0.61905 \sin(0.88253x) + 0.61905 \sinh(0.88253x) \\
 \varphi_{21} &= -0.50502 \cos(0.32749x - 1.5719) - 0.51603 \cosh(0.32749x - 1.5719) \\
 &\quad - 0.56726 \sin(0.32749x - 1.5719) - 0.36503 \sinh(0.32749x - 1.5719) \\
 \varphi_{22} &= 0.27913 \cos(0.83533x - 4.0096) + 0.33275 \cosh(0.83533x - 4.0096) \\
 &\quad + 0.81419 \sin(0.83533x - 4.0096) + 0.43633 \sinh(0.83533x - 4.0096)
 \end{aligned} \tag{A2}$$

3. Beam 3: $x = 2.4$ m, $L = 5$ m.

$$\begin{aligned}
 \varphi_{11} &= 0.61018 \cos(0.34802x) - 0.61018 \cosh(0.34802x) \\
 &\quad - 0.45149 \sin(0.34802x) + 0.45149 \sinh(0.34802x) \\
 \varphi_{12} &= 0.61018 \cos(0.88678x) - 0.61018 \cosh(0.88678x) \\
 &\quad - 0.62438 \sin(0.88678x) + 0.62438 \sinh(0.88678x) \\
 \varphi_{21} &= 0.017821 \cos(0.3294x - 0.79057) - 0.35632 \cosh(0.3294x - 0.79057) \\
 &\quad - 0.69923 \sin(0.3294x - 0.79057) - 0.048794 \sinh(0.3294x - 0.79057) \\
 \varphi_{22} &= 0.1012 \sinh(0.83936x - 2.0145) - 0.11156 \cosh(0.83936x - 2.0145) \\
 &\quad - 0.15858 \sin(0.83936x - 2.0145) - 0.75491 \cos(0.83936x - 2.0145) \\
 \varphi_{31} &= 0.022201 \cos(0.34802x - 0.90484) - 0.41077 \cosh(0.34802x - 0.90484) \\
 &\quad - 0.7516 \sin(0.34802x - 0.90484) + 0.021573 \sinh(0.34802x - 0.90484) \\
 \varphi_{32} &= 0.0064438 \cosh(0.88678x - 2.3056) - 0.87331 \cos(0.88678x - 2.3056) \\
 &\quad - 0.045001 \sin(0.88678x - 2.3056) + 0.095731 \sinh(0.88678x - 2.3056)
 \end{aligned} \tag{A3}$$

4. Beam 4: $x = 0$ m, $L = 5$ m.

$$\begin{aligned}
 \varphi_{11} &= 0.38382 \cos(0.33279x) - 0.38382 \cosh(0.33279x) \\
 &\quad - 0.29516 \sin(0.33279x) + 0.29516 \sinh(0.33279x) \\
 \varphi_{12} &= 0.38382 \cos(0.84617x) - 0.38382 \cosh(0.84617x) \\
 &\quad - 0.39268 \sin(0.84617x) + 0.39268 \sinh(0.84617x) \\
 \varphi_{21} &= 0.474 \cos(0.35159x - 0.070318) - 0.47568 \cosh(0.35159x - 0.070318) \\
 &\quad - 0.27384 \sin(0.35159x - 0.070318) + 0.22672 \sinh(0.35159x - 0.070318) \\
 \varphi_{22} &= 0.40864 \cos(0.89398x - 0.1788) - 0.419 \cosh(0.89398x - 0.1788) \\
 &\quad - 0.54041 \sin(0.89398x - 0.1788) + 0.42809 \sinh(0.89398x - 0.1788)
 \end{aligned} \tag{A4}$$

5. Beam 5: No actuator, $L = 3$ m.

$$\begin{aligned}
 \varphi_{11} &= 0.63817 \cos(0.55637x) - 0.63817 \cosh(0.55637x) \\
 &\quad - 0.47571 \sin(0.55637x) + 0.47571 \sinh(0.55637x) \\
 \varphi_{12} &= 0.63817 \cos(1.4424x) - 0.63817 \cosh(1.4424x) \\
 &\quad - 0.64792 \sin(1.4424x) + 0.64792 \sinh(1.4424x)
 \end{aligned} \tag{A5}$$

6. Beam 6: $x = 2.8$ m, $L = 3$ m.

$$\begin{aligned}
 \varphi_{11} &= 0.64439 \cos(0.55281x) - 0.64439 \cosh(0.55281x) \\
 &\quad - 0.48146 \sin(0.55281x) + 0.48146 \sinh(0.55281x) \\
 \varphi_{12} &= 0.64439 \cos(1.4397x) - 0.64439 \cosh(1.4397x) \\
 &\quad - 0.65404 \sin(1.4397x) + 0.65404 \sinh(1.4397x) \\
 \varphi_{21} &= -0.47078 \cos(0.52325x - 1.4651) - 0.49853 \cosh(0.52325x - 1.4651) \\
 &\quad - 0.64403 \sin(0.52325x - 1.4651) - 0.3264 \sinh(0.52325x - 1.4651) \\
 \varphi_{22} &= 0.1206 \cos(1.3627x - 3.8155) + 0.2418 \cosh(1.3627x - 3.8155) \\
 &\quad + 0.88655 \sin(1.3627x - 3.8155) + 0.37673 \sinh(1.3627x - 3.8155)
 \end{aligned} \tag{A6}$$

7. Beam 7: $x = 1.4$ m, $L = 3$ m.

$$\begin{aligned}
 \varphi_{11} &= 0.64665 \cos(0.55759x) - 0.64665 \cosh(0.55759x) \\
 &\quad - 0.48285 \sin(0.55759x) + 0.48285 * \sinh(0.55759x) \\
 \varphi_{12} &= 0.64665 \cos(1.4481x) - 0.64665 \cosh(1.4481x) \\
 &\quad - 0.66364 \sin(1.4481x) + 0.66364 \sinh(1.4481x) \\
 \varphi_{21} &= 0.054713 \cos(0.52777x - 0.73888) - 0.37258 \cosh(0.52777x - 0.73888) \\
 &\quad - 0.73512 \sin(0.52777x - 0.73888) - 0.023631 \sinh(0.52777x - 0.73888) \\
 \varphi_{22} &= 0.1053 \sinh(1.3706x - 1.9189) - 0.12186 \cosh(1.3706x - 1.9189) \\
 &\quad - 0.25016 \sin(1.3706x - 1.9189) - 0.78065 \cos(1.3706x - 1.9189) \\
 \varphi_{31} &= 0.030758 \cos(0.55759x - 0.89215) - 0.43096 \cosh(0.55759x - 0.89215) \\
 &\quad - 0.79426 \sin(0.55759x - 0.89215) + 0.037086 \sinh(0.55759x - 0.89215) \\
 \varphi_{32} &= 0.012452 \cosh(1.4481x - 2.3169) - 0.92891 \cos(1.4481x - 2.3169) \\
 &\quad - 0.043007 \sin(1.4481x - 2.3169) + 0.086512 \sinh(1.4481x - 2.3169)
 \end{aligned} \tag{A7}$$

8. Beam 8: $x = 0$ m, $L = 3$ m.

$$\begin{aligned}
 \varphi_{11} &= 0.41793 \cos(0.53618x) - 0.41793 \cosh(0.53618x) \\
 &\quad - 0.32157 \sin(0.53618x) + 0.32157 \sinh(0.53618x) \\
 \varphi_{12} &= 0.41793 \cos(1.3875x) - 0.41793 \cosh(1.3875x) \\
 &\quad - 0.41698 \sin(1.3875x) + 0.41698 \sinh(1.3875x) \\
 \varphi_{21} &= 0.49763 \cos(0.56647x - 0.11329) - 0.50231 \cosh(0.56647x - 0.11329) \\
 &\quad - 0.31329 \sin(0.56647x - 0.11329) + 0.23194 \sinh(0.56647x - 0.11329) \\
 \varphi_{22} &= 0.37958 \cos(1.4659x - 0.29317) - 0.40879 \cosh(1.4659x - 0.29317) \\
 &\quad - 0.60748 \sin(1.4659x - 0.29317) + 0.41832 \sinh(1.4659x - 0.29317)
 \end{aligned} \tag{A8}$$

where φ_{ij} is the j -th ($j = 1, 2$) mode of the i -th section of composite beam.

References

- Zhang, Z.; Li, X.; Li, Y.; Hu, G.; Wang, X.; Zhang, G.; Tao, H. Modularity, reconfigurability, and autonomy for the future in spacecraft: A review. *Chin. J. Aeronaut.* **2023**, *36*, 282–315. [\[CrossRef\]](#)
- Li, D.; Zhong, L.; Zhu, W.; Xu, Z.; Tang, Q.; Zhan, W. A Survey of Space Robotic Technologies for On-Orbit Assembly. *Space Sci. Technol.* **2022**, *2022*, 9849170. [\[CrossRef\]](#)
- Li, Y.K.; Li, S.; Xin, M. Dynamic Modeling and Attitude Control of Large-Scale Flexible Parallel Multibody Spacecraft. *J. Guid. Control Dyn.* **2022**, *45*, 2304–2317. [\[CrossRef\]](#)
- Cao, K.; Li, S.; She, Y.C.; Biggs, J.D.; Liu, Y.F.; Bian, L.L. Dynamics and on-orbit assembly strategies for an orb-shaped solar array. *Acta Astronaut.* **2021**, *178*, 881–893. [\[CrossRef\]](#)
- Li, Y.K.; Li, D.Y.; Zhu, W.S.; Sun, J.; Zhang, X.L.; Li, S. Constrained Motion Planning of 7-DOF Space Manipulator via Deep Reinforcement Learning Combined with Artificial Potential Field. *Aerospace* **2022**, *9*, 163. [\[CrossRef\]](#)
- Astone, P.; Bassan, M.; Bonifazi, P.; Carelli, P.; Coccia, E.; Fafone, V.; Febo, L.; Frasca, S.; Marini, A.; Mauceli, E.; et al. The Rome Group Resonant-Mass Detectors Explorer and Nautilus. In *Second Workshop Gravitational Wave Data Analysis*; Atlantica Séguier Frontières: Biarritz, France, 1997; p. 21.
- Li, J.; Zhang, L.; Li, S.; Mao, Q.; Mao, Y. Active disturbance rejection control for piezoelectric smart structures: A review. *Machines* **2023**, *11*, 174. [\[CrossRef\]](#)
- da Fonseca, I.M.; Rade, D.A.; Goes, L.C.; de Paula Sales, T. Attitude and vibration control of a satellite containing flexible solar arrays by using reaction wheels, and piezoelectric transducers as sensors and actuators. *Acta Astronaut.* **2017**, *139*, 357–366. [\[CrossRef\]](#)
- Callipari, F.; Sabatini, M.; Angeletti, F.; Iannelli, P.; Gasbarri, P. Active vibration control of large space structures: Modelling and experimental testing of offset piezoelectric stack actuators. *Acta Astronaut.* **2022**, *198*, 733–745. [\[CrossRef\]](#)
- Qing, X.; Li, W.; Wang, Y.; Sun, H. Piezoelectric transducer-based structural health monitoring for aircraft applications. *Sensors* **2019**, *19*, 545. [\[CrossRef\]](#)
- Liu, X.; Cai, G.; Peng, F.; Zhang, H. Dynamic model and active vibration control of a membrane antenna structure. *J. Vib. Control* **2018**, *24*, 4282–4296. [\[CrossRef\]](#)
- Zorić, N.D.; Tomović, A.M.; Obradović, A.M.; Radulović, R.D.; Petrović, G.R. Active vibration control of smart composite plates using optimized self-tuning fuzzy logic controller with optimization of placement, sizing and orientation of PFRC actuators. *J. Sound Vib.* **2019**, *456*, 173–198. [\[CrossRef\]](#)

13. Yang, C.; Zhang, X.; Huang, X.; Cheng, Z.; Zhang, X.; Hou, X. Optimal sensor placement for deployable antenna module health monitoring in SSPS using genetic algorithm. *Acta Astronaut.* **2017**, *140*, 213–224. [[CrossRef](#)]
14. Angeletti, F.; Gasbarri, P.; Sabatini, M. Optimal design and robust analysis of a net of active devices for micro-vibration control of an on-orbit large space antenna. *Acta Astronaut.* **2019**, *164*, 241–253. [[CrossRef](#)]
15. Goncalves, J.F.; De Leon, D.M.; Perondi, E.A. Topology optimization of embedded piezoelectric actuators considering control spillover effects. *J. Sound Vib.* **2017**, *388*, 20–41. [[CrossRef](#)]
16. Rad, H.K.; Salarieh, H.; Alasty, A.; Vatankehah, R. Boundary control of anti-symmetric vibration of satellite with flexible appendages in planar motion with exponential stability. *Acta Astronaut.* **2018**, *147*, 219–230. [[CrossRef](#)]
17. Ataei, M.M.; Salarieh, H.; Pishkenari, H.N.; Jalili, H. Boundary control design for vibration suppression and attitude control of flexible satellites with multi-section appendages. *Acta Astronaut.* **2020**, *173*, 22–30. [[CrossRef](#)]
18. Chen, T.; Wen, H.; Wei, Z.T. Distributed attitude tracking for multiple flexible spacecraft described by partial differential equations. *Acta Astronaut.* **2019**, *159*, 637–645. [[CrossRef](#)]
19. Li, W.P.; Huang, H. Integrated optimization of actuator placement and vibration control for piezoelectric adaptive trusses. *J. Sound Vib.* **2013**, *332*, 17–32. [[CrossRef](#)]
20. Angeletti, F.; Iannelli, P.; Gasbarri, P.; Sabatini, M. End-to-end design of a robust attitude control and vibration suppression system for large space smart structures. *Acta Astronaut.* **2021**, *187*, 416–428. [[CrossRef](#)]
21. Biglar, M.; Gromada, M.; Stachowicz, F.; Trzecieński, T. Optimal configuration of piezoelectric sensors and actuators for active vibration control of a plate using a genetic algorithm. *Acta Mech.* **2015**, *226*, 3451–3462. [[CrossRef](#)]
22. Bruant, I.; Proslie, L. Optimal location of piezoelectric actuators for active vibration control of thin axially functionally graded beams. *Int. J. Mech. Mater. Des.* **2016**, *12*, 173–192. [[CrossRef](#)]
23. Liu, X.; Cai, G.P.; Peng, F.J.; Zhang, H. Piezoelectric Actuator Placement Optimization and Active Vibration Control of a Membrane Structure. *Acta Mech. Solida Sin.* **2018**, *31*, 66–79. [[CrossRef](#)]
24. Cao, K.; Li, S.; Li, Y.K.; Xin, M. Dynamic Modeling and Distributed Control of Asymmetric Flexible Spacecraft. *J. Guid. Control Dyn.* **2022**, *46*, 141–151. [[CrossRef](#)]
25. Nakka, Y.K.; Chung, S.J.; Allison, J.T.; Aldrich, J.B.; Alvarez-Salazar, O.S. Nonlinear Attitude Control of a Spacecraft with Distributed Actuation of Solar Arrays. *J. Guid. Control Dyn.* **2019**, *42*, 458–475. [[CrossRef](#)]
26. Meirovitch, L. *Fundamentals of Vibrations*; McGraw-Hill: Boston, MA, USA, 2001.
27. Leleu, S.; Abou-Kandil, H.; Bonnassieux, Y. Piezoelectric actuators and sensors location for active control of flexible structures. In Proceedings of the 17th IEEE Instrumentation and Measurement Technology Conference, Baltimore, MD, USA, 1–4 May 2000; Volume 2, pp. 818–823.
28. Moheimani, S.O.R.; Ryall, T.G. Considerations on placement of piezoceramic actuators that are used in structural vibration control. In Proceedings of the 38th IEEE Conference on Decision and Control (Cat. No. 99CH36304), Phoenix, AZ, USA, 7–10 December 1999; Volume 2, pp. 1118–1123.

Disclaimer/Publisher’s Note: The statements, opinions and data contained in all publications are solely those of the individual author(s) and contributor(s) and not of MDPI and/or the editor(s). MDPI and/or the editor(s) disclaim responsibility for any injury to people or property resulting from any ideas, methods, instructions or products referred to in the content.